

## Measuring the Innermost Stable Circular Orbits of Supermassive Black Holes

G. Chartas<sup>1,2</sup>, H. Krawczynski<sup>3</sup>, L. Zalesky<sup>1</sup>, C. S. Kochanek<sup>4,5</sup>, X. Dai<sup>6</sup>, C. W. Morgan<sup>7</sup>, and A. Mosquera<sup>7</sup>
Department of Physics and Astronomy, College of Charleston, Charleston, SC 29424, USA; chartasg@cofc.edu

Department of Physics and Astronomy, University of South Carolina, Columbia, SC 29208, USA

Physics Department and McDonnell Center for the Space Sciences, Washington University in St. Louis, 1 Brookings Drive, CB 1105, St. Louis, MO 63130, USA

Department of Astronomy, The Ohio State University, 140 West 18th Avenue, Columbus, OH 43210, USA

Center for Cosmology and AstroParticle Physics, The Ohio State University, 191 W. Woodruff Avenue, Columbus, OH 43210, USA

Homer L. Dodge Department of Physics and Astronomy, University of Oklahoma, Norman, OK 73019, USA

Physics Department, United States Naval Academy, Annapolis, MD 21403, USA

Received 2016 September 19; revised 2017 January 20; accepted 2017 January 29; published 2017 February 28

## Abstract

We present a promising new technique, the *g*-distribution method, for measuring the inclination angle (*i*), the innermost stable circular orbit (ISCO), and the spin of a supermassive black hole. The *g*-distribution method uses measurements of the energy shifts in the relativistic iron line emitted by the accretion disk of a supermassive black hole due to microlensing by stars in a foreground galaxy relative to the *g*-distribution shifts predicted from microlensing caustic calculations. We apply the method to the gravitationally lensed quasars RX J1131–1231 ( $z_s = 0.658$ ,  $z_l = 0.295$ ), QJ 0158–4325 ( $z_s = 1.294$ ,  $z_l = 0.317$ ), and SDSS 1004+4112 ( $z_s = 1.734$ ,  $z_l = 0.68$ ). For RX J1131–1231, our initial results indicate that  $r_{\rm ISCO} \lesssim 8.5$  gravitational radii ( $r_g$ ) and  $i \gtrsim 55^\circ$  (99% confidence level). We detect two shifted Fe lines in several observations, as predicted in our numerical simulations of caustic crossings. The current  $\Delta E$  distribution of RX J1131–1231 is sparsely sampled, but further X-ray monitoring of RX J1131–1231 and other lensed quasars will provide improved constraints on the inclination angles, ISCO radii, and spins of the black holes of distant quasars.

Key words: accretion, accretion disks – black hole physics – galaxies: active – gravitational lensing: micro

## 1. Introduction

One technique for measuring the innermost stable circular orbit (ISCO) and spin parameter a ( $a = Jc/GM_{BH}^2$ , where J is the angular momentum) of active galactic nuclei (AGNs) relies on modeling the relativistically blurred Fe K $\alpha$  fluorescence lines originating from the inner parts of the disk (e.g., Fabian et al. 1989; Laor 1991; Reynolds & Nowak 2003). This relativistic iron line method has be applied to about 20 relatively bright, nearby Seyferts where the line is detectable with a high signal-to-noise ratio (S/N; Reynolds 2014 and Vasudevan et al. 2016). The sample sizes are starting to become large enough where the distribution of the spin parameter can be calculated and compared to simulated ones such as those presented in Volonteri et al. (2013). Even then, the Fe K $\alpha$  line in most Seyferts is typically very weak, and constraining the spin and accretion disk parameters of Seyferts requires considerable observing time on XMM-Newton and Chandra. Moreover, the accuracy of the relativistic Fe line method for constraining the spin of a black hole from the broadened red wing of the Fe line profile is also questioned (e.g., Miller et al. 2009; Sim et al. 2012). We note, however, that independent measurements of the size of the corona from microlensing and reverberation mapping indicate that the X-ray source is compact, consistent with the lamppost model assumed in the relativistic Fe iron line method. Additional support for the relativistic Fe line method is provided by 3–50 keV observations with NuSTAR, such as the recent observations of Mrk 335 that indicate a spin parameter of >0.9 at  $3\sigma$ confidence. The high-energy NuSTAR spectra can help to constrain the reflection component and better distinguish between models (Parker et al. 2014). Most of the measured spin parameters in Seyfert galaxies are found to be  $\gtrsim 0.9$  (e.g., Reynolds 2014 and references therein). This may be the result of a selection bias in flux-limited samples (Vasudevan et al. 2016). Specifically, high-spin black holes are more luminous and hence brighter for a given accretion rate, and therefore will simply be more highly represented in flux-limited surveys. Recent observations and simulations (Fabian 2014; Keck et al. 2015; Vasudevan et al. 2016) also suggest that rapidly spinning black holes will tend to have stronger reflected relative to direct X-ray emission, making it easier to measure the spin parameter in these objects.

The relativistic iron line method has been applied to the gravitationally lensed quasars RX J1131–1231 (Reis et al. 2014) and Q2237+0305 (Reynolds et al. 2014), as well as to a stacked spectrum of 27 lensed 1.0 < z < 4.5 quasars observed with *Chandra* (Walton et al. 2015). Specifically, the relativistic disk reflection features were fit with standard relativistic Fe K $\alpha$  models to infer inclination angles and spin parameters of  $i=15^{\circ+9^{\circ}}_{-15^{\circ}}$  and  $a=0.87^{+0.08}_{-0.15}$  for RX J1131–1231 (Reis et al. 2014) and  $i\lesssim11^{\circ}.5$  and  $a=0.74^{+0.06}_{-0.03}$  for Q2237+0305 (Reynolds et al. 2014).

These studies have not, however, correctly accounted for the effects of gravitational microlensing. Gravitational microlensing is a well-studied phenomenon in lensed quasars (e.g., see the review by Wambsganss 2006, and references therein) where stars near the lensed images produce time-variable magnification of source components whose amplitude depends on the location and size of the emission region. In particular, in our analysis of the X-ray spectra of lensed quasars (Chartas et al. 2016), we have frequently observed structural changes in the Fe  $K\alpha$  emission, indicating that the line emission is being differentially microlensed. Thus, applying the relativistic Fe  $K\alpha$  line method to stacked spectra of lensed quasars, without accurately accounting for microlensing, is likely to lead to unreliable and unrealistic results.

In Section 2 we present the X-ray observations and analyses of the *Chandra* observations of RX J1131–1231, OJ 0158-4325, and SDSS 1004+4112. In Section 3 we discuss our recently developed technique based on microlensing to provide a robust constraint on the inclination angle, the location of the ISCO, and the spin parameter, and we present an analytic estimate of the fractional energy shifts  $g = E_{\rm obs}/E_{\rm rest}$  and numerical simulations of microlensing events. In Section 4 we present our results from modeling the observed distribution of g and the distribution of the measured energy separations of shifted Fe K $\alpha$  lines in cases where two shifted lines are detected in an individual spectrum. Finally, in Section 5 we rule out several alternative scenarios to explain the shifted iron lines and present a summary of our conclusions. Throughout this paper we adopt a flat  $\Lambda$  cosmology with  $H_0 = 67 \, \mathrm{km \, s^{-1} \, Mpc^{-1}}$ ,  $\Omega_{\Lambda} = 0.69$ , and  $\Omega_{\rm M}=0.31$  (Planck Collaboration et al. 2016).

## 2. X-Ray Observation and Data Analysis

We have performed multiwavelength monitoring of several gravitationally lensed quasars (e.g., see Table 1 of Chartas et al. 2016 and references within) with the main scientific goal of measuring the emission structure near the black holes in the optical, UV, and X-ray bands in order to test accretion disk models. The X-ray monitoring observations were performed with the *Chandra X-ray Observatory* (hereafter *Chandra*). The optical observations (B, R, and I bands) were made with the SMARTS Consortium 1.3 m telescope in Chile. The UV observations were performed with the *Hubble Space Telescope*. In this paper we focus on constraining the inclination angles, ISCO radii, and spin parameters of quasars RX J1131–1231, QJ 0158–4325, and SDSS 1004+4112 using the *Chandra* observations of these objects.

RX J1131-1231 (hereafter RXJ1131) was observed with the Advanced CCD Imaging Spectrometer (ACIS; Garmire et al. 2003) on board the Chandra X-ray Observatory 38 times between 2004 April 12 and 2014 July 12. Results from the analysis of observations 1-6 of RXJ1131 were presented in Chartas et al. (2009) and Dai et al. (2010), and those for observations 7-29 are in Chartas et al. (2012). Results from the analysis of a subset of these observations have also been presented in Blackburne et al. (2006), Kochanek et al. (2007), and Pooley et al. (2012). Here we describe the data analysis for the remaining nine observations, but we will use the results from all 38 observations in our microlensing analysis. QJ 0158-4325 (hereafter QJ0158) was observed with ACIS 12 times between 2010 November 6 and 2015 June 10, and SDSS 1004+4112 (hereafter SDSS1004) was observed with ACIS 10 times between 2005 January 1 and 2014 June 2. Results from the analysis of the first six observations of QJ0158 and the first five observations of SDSS1004 were presented in Chen et al. (2012).

We reanalyzed all of the *Chandra* observations of RXJ1131, QJ0158, and SDSS1004 using the software CIAO 4.8 with CALDB version 4.7.2, provided by the *Chandra X-ray Center (CXC)*. Logs of the observations for each object in our study that include observation dates, observation identification numbers, exposure times, ACIS frame times, and the observed 0.2–10 keV counts are presented in Tables 1–3. The properties of our sample are presented in Table 4. We used standard *CXC* threads to screen the data for status, grade, and time intervals of acceptable aspect solution and background levels.

In Figures 1–3 we show the 0.2–10 keV light curves of the images of RXJ1131, QJ0158, and SDSS1004. The light curves have been shifted by the time delays estimated by Tewes et al. (2013), Faure et al. (2009), and Fohlmeister et al. (2008), respectively. Microlensing will affect the images differently, resulting in uncorrelated variability between images. Large uncorrelated events are noticeably present in the images of RXJ1131, QJ0158, and SDSS1004, indicating that the X-ray emission regions are significantly smaller than the projected Einstein radius of the stars and thus are affected by microlensing (e.g., Chartas et al. 1995, 2009; Dai et al. 2003, 2010; Blackburne et al. 2006; Pooley et al. 2007; Mosquera et al. 2013).

For the spectral analyses, we followed the approach described in Chartas et al. (2012). We extracted events from circular regions with radii of 1.5 arcsec slightly off center from the images to reduce contamination from nearby images. The backgrounds were determined by extracting events within an annulus centered on the mean location of the images with inner and outer radii of 7.5 arcsec and 50 arcsec, respectively. Spectral fits were restricted to events with energies in the range 0.4–10 keV. Spectra with fewer than  $\sim$ 200 counts were fit using the C statistic (Cash 1979), as appropriate for fitting spectra with low S/N. Spectra with a larger number of counts were fit using both the C and  $\chi^2$  statistics.

We fit the Chandra spectra for each epoch with a model that consists of a power law with neutral intrinsic absorption at the redshift of the source. Galactic column densities in the directions of RXJ1131, QJ0158, and SDSS1004 were fixed to  $N_{\rm H} =$  $3.60 \times 10^{20} \,\mathrm{cm^{-2}}, \ N_{\mathrm{H}} = 1.88 \times 10^{20} \,\mathrm{cm^{-2}}, \ \mathrm{and} \ N_{\mathrm{H}} = 1.13 \times 10^{20} \,\mathrm{cm^{-2}}, \ \mathrm{respectively}$  (Dickey & Lockman 1990). Measurements of the differential X-ray absorption between images in lensed quasars SBS 0909+523, FBQS 0951+2635, and B 1152 +199 by Dai & Kochanek (2009) have been used to successfully constrain the dust-to-gas ratio of the lens galaxies, and we plan to present the application of this method to our lens sample in a future paper. We next added one or two Gaussian emission lines to the model and tested for the significance of the added lines. The significance of the emission lines was determined by varying the energy and width of the iron line and its flux to calculate the  $\chi^2$  of the fit as a function of the Fe line energy and iron line flux. In several cases, two emission lines are detected in a single spectrum. We record all cases where one or more emission lines are detected above the 90% and 99% confidence levels. Note that all these lines are detected in single epochs and not from stacked observations.

The confidence levels between the iron line flux and energy were created using the steppar command in XSPEC. As pointed out by Protassov et al. (2002), this approach may not apply for models near a boundary, such as in cases where the line flux normalization is constrained to have only positive values. To account for this limitation, we allowed the line flux normalization to obtain both positive and negative values. Protassov et al. (2002) proposed a more robust approach of estimating the significance of the shifted iron line based on Monte Carlo simulations to determine the distribution of the F statistic between different models. We followed this approach and constructed the simulated probability density distribution of the F statistic between spectral fits of models that included a simple absorbed power law (null model), and one that

The spectra were binned to have at least one count per bin.

**Table 1**Log of Observations of Quasar RX J1131–1231

Epoch	Observation	$ m JD^a$	Chandra Observation	Exposure Time	$t_{ m f}^{ m b}$	$N_{ m A}{}^{ m c}$	$N_{ m B}{}^{ m c}$	$N_{ m C}{}^{ m c}$	$N_{\rm D}^{\rm c}$
Lpoen	Date	(days)	ID	(ks)	(s)	counts	counts	counts	counts
1	2004 Apr 12	3108	4814	10.0	3.14	425 <sup>+22</sup> <sub>-22</sub>	2950+54	839+29	211+15
2	2006 Mar 10	3805	6913	4.9	0.741	$393^{+20}_{-20}$	$624_{-25}^{+25}$	$204_{-14}^{+14}$	$103^{+10}_{-10}$
3	2006 Mar 15	3810	6912	4.4	0.741	$381^{+20}_{-20}$	$616^{+25}_{-25}$	$233^{+15}_{-15}$	$93^{+10}_{-10}$
4	2006 Apr 12	3838	6914	4.9	0.741	$413^{+20}_{-20}$	$507^{+23}_{-23}$	$146^{+12}_{-12}$	$131^{+12}_{-12}$
5	2006 Nov 10	4050	6915	4.8	0.741	$3708^{+61}_{-61}$	$1411^{+38}_{-38}$	$367^{+19}_{-19}$	$155^{+13}_{-13}$
6	2006 Nov 13	4053	6916	4.8	0.741	$3833^{+62}_{-62}$	$1618_{-40}^{+40}$	$415^{+20}_{-20}$	$115^{+11}_{-11}$
7	2006 Dec 17	4087	7786	4.88	0.841	$3541^{+102}_{-99}$	$1443^{+59}_{-58}$	$417^{+29}_{-28}$	$117^{+15}_{-13}$
8	2007 Jan 01	4102	7785	4.70	0.441	$2305_{-74}^{+75}$	$1082^{+51}_{-49}$	$312^{+26}_{-25}$	$108^{+15}_{-13}$
9	2007 Feb 13	4145	7787	4.71	0.441	$2451_{-78}^{+79}$	$1116_{-49}^{+51}$	$301^{+25}_{-24}$	$169^{+18}_{-17}$
10	2007 Feb 18	4150	7788	4.43	0.441	$2232_{-73}^{+75}$	$950^{+47}_{-45}$	$252^{+23}_{-22}$	$115^{+15}_{-14}$
11	2007 Apr 16	4207	7789	4.71	0.441	$2328_{-74}^{+74}$	$1202_{-53}^{+54}$	$344^{+27}_{-26}$	$99^{+14}_{-12}$
12	2007 Apr 25	4216	7790	4.70	0.441	$2043_{-70}^{+67}$	$1063^{+50}_{-48}$	$363^{+28}_{-26}$	$142^{+17}_{-16}$
13	2007 Jun 04	4256	7791	4.66	0.441	$2079_{-69}^{+70}$	$1480^{+60}_{-59}$	$373^{+28}_{-27}$	$108^{+15}_{-13}$
14	2007 Jun 11	4263	7792	4.68	0.441	$2254_{-72}^{+73}$	$1466^{+58}_{-56}$	$337^{+26}_{-25}$	$129^{+16}_{-15}$
15	2007 Jul 24	4306	7793	4.67	0.441	$1958^{+69}_{-68}$	$1324_{-55}^{+57}$	$353^{+27}_{-25}$	$81^{+12}_{-11}$
16	2007 Jul 30	4312	7794	4.67	0.441	$2725^{+80}_{-79}$	$1844^{+69}_{-67}$	$496^{+32}_{-31}$	$100^{+13}_{-12}$
17	2008 Mar 16	4542	9180	14.32	0.741	$5557^{+118}_{-117}$	$4347^{+105}_{-104}$	$1337^{+53}_{-51}$	$351^{+25}_{-24}$
18	2008 Apr 13	4570	9181	14.35	0.741	$8199^{+147}_{-147}$	$5654^{+118}_{-117}$	$1453^{+52}_{-52}$	$377^{+25}_{-24}$
19	2008 Apr 23	4580	9237	14.31	0.741	$6786^{+130}_{-130}$	$4927^{+112}_{-111}$	$1279^{+51}_{-51}$	$232^{+21}_{-20}$
20	2008 Jun 01	4619	9238	14.24	0.741	$4647^{+108}_{-106}$	$3252_{-88}^{+90}$	$878^{+43}_{-41}$	$463^{+28}_{-27}$
21	2008 Jul 05	4653	9239	14.28	0.741	$5587^{+119}_{-118}$	$3584_{-94}^{+95}$	$1001_{-44}^{+44}$	$635^{+33}_{-32}$
22	2008 Nov 11	4782	9240	14.30	0.741	$5135^{+115}_{-113}$	$3085_{-85}^{+87}$	$885^{+44}_{-42}$	$488^{+30}_{-29}$
23	2009 Nov 28	5164	11540	27.52	0.741	$36024_{-340}^{+342}$	$7357^{+126}_{-128}$	$2420_{-68}^{+68}$	$3827^{+82}_{-81}$
24	2010 Feb 09	5237	11541	25.62	0.741	$26850^{+281}_{-290}$	$5814^{+117}_{-117}$	$2059_{-81}^{+86}$	$2437_{-88}^{+79}$
25	2010 Apr 17	5304	11542	25.67	0.741	$20935^{+246}_{-245}$	$6124^{+120}_{-119}$	$1962^{+62}_{-62}$	$2813_{-69}^{+70}$
26	2010 Jun 25	5373	11543	24.62	0.741	$18521^{+230}_{-228}$	$5445^{+111}_{-111}$	$1522^{+54}_{-54}$	$1487^{+51}_{-51}$
27	2010 Nov 11	5512	11544	25.56	0.741	$27077^{+298}_{-467}$	$6316^{+120}_{-158}$	$1821^{+57}_{-64}$	$1730^{+56}_{-59}$
28	2011 Jan 21	5583	11545	24.62	0.741	$5689^{+153}_{-164}$	$3175^{+111}_{-123}$	$1008^{+47}_{-53}$	$982^{+47}_{-46}$
29	2011 Feb 25	5618	12833	13.61	0.441	$5412_{-165}^{+159}$	$4375^{+131}_{-128}$	$1161^{+52}_{-52}$	$821^{+44}_{-41}$
30	2011 Nov 9	5875	12834	13.61	0.441	$2206_{-77}^{+77}$	$2929^{+104}_{-104}$	$633^{+37}_{-37}$	$210^{+18}_{-18}$
31	2012 Apr 11	6229	13962	13.67	0.441	$2557^{+99}_{-99}$	$3660^{+107}_{-107}$	$730^{+39}_{-39}$	$480^{+27}_{-27}$
32	2012 Nov 7	6239	13963	14.57	0.441	$1521_{-73}^{+73}$	$2174^{+105}_{-105}$	$504^{+33}_{-33}$	$270^{+22}_{-22}$
33	2012 Nov 18	6250	14507	9.13	0.441	$738^{+59}_{-59}$	$1068^{+70}_{-70}$	$262_{-27}^{+27}$	$169^{+17}_{-17}$
34	2012 Dec 12	6274	14508	9.13	0.441	$1163^{+203}_{-73}$	$1518^{+98}_{-158}$	$399^{+34}_{-47}$	$187^{+49}_{-19}$
35	2013 Nov 30	6627	14509	9.13	0.441	$1420^{+100}_{-80}$	$1649^{+89}_{-111}$	$649_{-44}^{+41}$	$347^{+36}_{-29}$
36	2014 Jan 3	6661	14510	8.75	0.441	$1374^{+69}_{-76}$	$1344^{+88}_{-89}$	$441^{+32}_{-30}$	$322^{+34}_{-30}$
37	2014 Jun 13	6822	14511	9.13	0.441	$1352_{-70}^{+75}$	$1795^{+95}_{-122}$	$525^{+36}_{-36}$	$296^{+31}_{-26}$
38	2014 Jul 7	6851	14512	10.04	0.441	$806^{+76}_{-68}$	$1132^{+88}_{-92}$	$392^{+42}_{-42}$	$317^{+31}_{-29}$

included one or two Gaussian emission lines (alternative model). Specifically, for each observed spectrum, we simulated 1000 data sets using the XSPEC fakeit command. We fit the null and alternative models to the 1000 simulated data sets and computed the F statistic for each fit. Finally from the Monte Carlo simulations we computed the probability of obtaining an F value larger than the one obtained from the fits of the null and alternative models to the observed spectrum. In Tables 5–7 we provide the F statistic between the null and alternative models and the probability of exceeding this value as determined from the Monte Carlo simulations.

In Figure 4 we show a typical example of the Monte Carlo simulated distribution of the F statistic between fits of the null and alternative models to the observed spectrum of image C of RXJ1131 obtained in 2009 November 28 (obsid = 11540). We find that in this spectrum the probability of obtaining an F value larger than 2.69 is P=0.018. In all cases listed in Tables 5–7, we confirm the significance of the shifted lines, and in all cases the significance inferred from the Monte Carlo analysis is similar or larger than the lower limits provided by the 90% and 99%  $\chi^2$  confidence contours.

In Figures 5–7 we show typical examples of Fe K $\alpha$  lines detected in the spectra of individual images and epochs from

<sup>&</sup>lt;sup>a</sup> Julian Date-2450000.

<sup>&</sup>lt;sup>b</sup> ACIS frame time.

<sup>&</sup>lt;sup>c</sup> Background-subtracted source counts for events with energies in the 0.2–10 keV band. The counts for images A and B of RX J1131–1231 are corrected for pileup. Images C and D are not affected by pileup.

**Table 2**Log of Observations of Quasar Q J0158–4325

Epoch	Observation Date	JD <sup>a</sup> (days)	Chandra Observation ID	Exposure Time (ks)	<i>t</i> <sub>f</sub> <sup>b</sup> (s)	N <sub>soft,A</sub> <sup>c</sup> counts	N <sub>soft,B</sub> <sup>c</sup> counts	N <sub>hard,A</sub> <sup>c</sup> counts	N <sub>hard,B</sub> <sup>c</sup> counts
1	2009 Nov 06	5142	11556	5.03	1.74	103 ± 10	43 ± 7	35 ± 6	11 ± 3
2	2010 Jan 12	5209	11557	5.02	1.74	$125\pm11$	$61 \pm 8$	$35 \pm 6$	$19 \pm 4$
3	2010 Mar 10	5266	11558	5.04	1.74	$146 \pm 12$	$48 \pm 7$	$38 \pm 6$	$8\pm3$
4	2010 May 23	5340	11559	4.94	1.74	$131 \pm 11$	$38 \pm 6$	$38 \pm 6$	$10\pm3$
5	2010 Jul 28	5406	11560	4.95	1.74	$144 \pm 12$	$34 \pm 6$	$35 \pm 6$	$7\pm3$
6	2010 Oct 06	5476	11561	4.94	1.74	$122 \pm 11$	$39 \pm 6$	$28 \pm 5$	$14 \pm 4$
7	2013 Mar 26	6378	14483	18.62	1.74	$375\pm19$	$100 \pm 10$	$110 \pm 10$	$24 \pm 5$
8	2013 Apr 24	6407	14484	18.62	1.74	$314 \pm 18$	$93 \pm 10$	$90 \pm 10$	$34 \pm 6$
9	2013 Dec 5	6632	14485	18.62	1.74	$458\pm21$	$99 \pm 10$	$119 \pm 11$	$31 \pm 6$
10	2013 Dec 28	6655	14486	18.61	1.74	$339 \pm 18$	$134 \pm 12$	$138 \pm 12$	$45\pm7$
11	2014 May 29	6807	14487	18.62	1.74	$557\pm24$	$137 \pm 13$	$166 \pm 13$	$59\pm8$
12	2014 Jun 10	6819	14488	18.62	1.74	$520\pm23$	$163\pm12$	$150\pm12$	$55\pm7$

 Table 3

 Log of Observations of Quasar SDSS 1004+4112

Epoch	Observation Date	JD <sup>a</sup> (days)	<i>Chandra</i> <sup>b</sup> ObsID	Time <sup>c</sup> (ks)	$N_{ m A}{}^{ m d}$ counts	$N_{ m B}^{ m d}$ counts	$N_{\rm C}^{\rm d}$ counts	$N_{\rm D}^{\rm d}$ counts
1	2010 Mar 8	5264	11546	5.96	$53 \pm 7(16 \pm 4)$	82 ± 9(19 ± 4)	66 ± 8(20 ± 4)	$90 \pm 9(20 \pm 4)$
2	2010 Jun 19	5367	11547	5.96	$44 \pm 7(16 \pm 4)$	$44 \pm 7(15 \pm 4)$	$97 \pm 10(29 \pm 5)$	$84 \pm 9(14 \pm 4)$
3	2010 Sep 23	5463	11548	5.96	$51 \pm 7(13 \pm 4)$	$65 \pm 8(17 \pm 4)$	$66 \pm 8(22 \pm 5)$	$58 \pm 8(20 \pm 4)$
4	2011 Jan 30	5592	11549	5.96	$29 \pm 5(7 \pm 3)$	$36 \pm 6(14 \pm 4)$	$115 \pm 11(27 \pm 5)$	$85 \pm 9(28 \pm 5)$
5	2013 Jan 27	6320	14495	24.74	$192 \pm 14(60 \pm 8)$	$425 \pm 21(118 \pm 11)$	$360 \pm 19(94 \pm 10)$	$223 \pm 15(74 \pm 9)$
6	2013 Mar 1	6353	14496	24.74	$164 \pm 13(88 \pm 9)$	$414 \pm 20(139 \pm 12)$	$338 \pm 18(124 \pm 11)$	$184 \pm 14(83 \pm 9)$
7	2013 Oct 5	6571	14497	24.13	$179 \pm 13(87 \pm 9)$	$355 \pm 19(97 \pm 10)$	$356 \pm 19(114 \pm 11)$	$182 \pm 14(48 \pm 7)$
8	2013 Nov 16	6613	14498	23.75	$171 \pm 13(53 \pm 7)$	$358 \pm 19(98 \pm 10)$	$406 \pm 20(92 \pm 10)$	$250 \pm 16(83 \pm 9)$
9	2014 Apr 29	6777	14499	23.32	$139 \pm 12(65 \pm 8)$	$284 \pm 17(94 \pm 10)$	$245 \pm 16(82 \pm 9)$	$151 \pm 12(59 \pm 8)$
10	2014 Jun 2	6811	14500	24.74	$132 \pm 11(56 \pm 8)$	$422 \pm 21(132 \pm 11)$	$261 \pm 16(85 \pm 9)$	$138 \pm 12(45 \pm 7)$

Notes. The ACIS-S frame-time for all observations is 3.1 s.

**Table 4** Properties of Samples

Object	$Z_S$	$z_l$	$L_{ m Bol}/L_{ m Edd}$	$\log(M_{ m BH}) \ (M_{\odot})$	log(R <sub>E</sub> ) (cm)	$log(r_g)$ (cm)	$R_E/v_e$ (years)	$\frac{10r_g/v_e}{\text{(months)}}$	$(\text{km s}^{-1})$	μ
RXJ1131	0.658	0.295	0.01-0.42	7.9–8.3	16.4	13.1–13.5	11.1	0.64-1.6	720	57
QJ0158	1.29	0.317	0.4	8.2	16.5	13.4	18.0	1.5	600	5
SDSS1004	1.73	0.68	0.05	8.6	16.4	13.8	9.4	2.9	785	70

Note.  $M_{\rm BH}$  and  $R_{\rm E}$  are the black hole mass and Einstein radius ( $\langle {\rm M} \rangle = 0.3~M_{\odot}$ ) with  $r_{\rm g} = {\rm G}M_{\rm BH}/c^2$ .  $R_{\rm E}/v_e$  and  $r_{\rm g}/v_e$  are the crossing times given the effective velocity  $v_e$  (see Mosquera & Kochanek 2011).  $\mu$  is the total flux magnification of the background quasar. For the estimate of the Eddington ratios, we assumed a 2–10 keV bolometric correction factor of  $\kappa_{2-10~{\rm keV}} \sim 30$ .

RXJ1131, QJ0158, and SDSS1004, respectively. We also show the respective  $\chi^2$  contours of the detected lines. Tables 5–7 provide the line and continuum properties for all these detections. For RX J1131 we have 78 line detections out of

the 152 spectra (38 epochs  $\times$  4 images) at >90% confidence, of which 21 lines are detected at >99% confidence. For the six *Chandra* observations of QJ0158 with exposure times of  $\sim$ 19 ks, we detect 10 iron lines in 12 spectra (6 epochs  $\times$  2

<sup>&</sup>lt;sup>a</sup> Julian Date-2450000.

b ACIS frame time.

<sup>&</sup>lt;sup>c</sup> Background-subtracted source counts for events with energies in the 0.2-10 keV band.

<sup>&</sup>lt;sup>a</sup> Julian Date-2450000.

<sup>&</sup>lt;sup>b</sup> Observation ID.

<sup>&</sup>lt;sup>c</sup> Effective exposure time after applying filters.

<sup>&</sup>lt;sup>d</sup> Soft band: 0.2–2 keV; hard band: 2–10 keV counts.

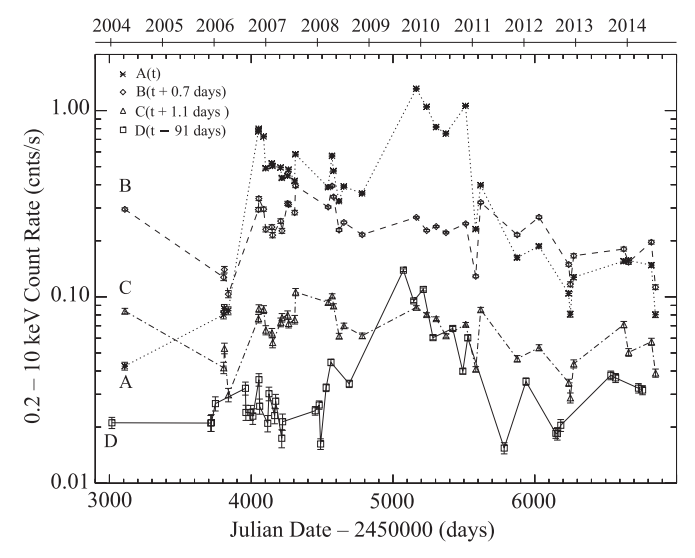


**Figure 1.** Total (0.2–10 keV) light curves of images A, B, C, and D of RX J1131–1231 shifted by the time delays estimated by Tewes et al. (2013). The total counts for images A and B have been corrected for pileup effects, while pileup is unimportant for images C and D. The new X-ray data begin after epoch 29 (2011 February, JD–2450000 = 5618).

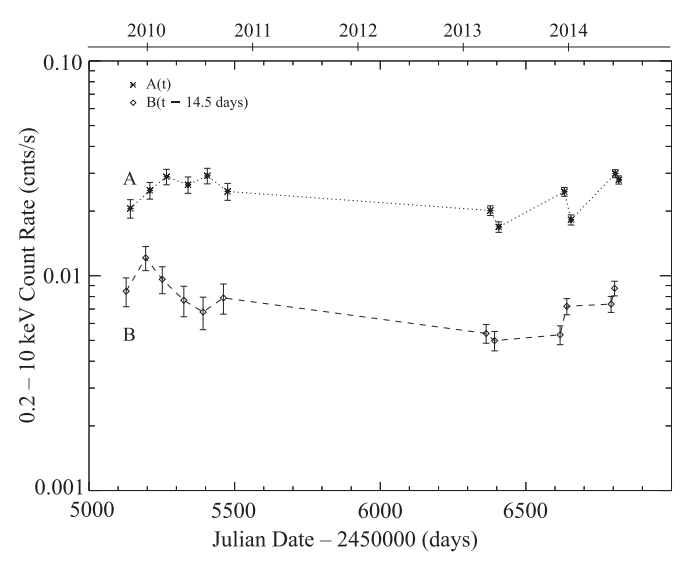


**Figure 2.** Total (0.2–10 keV) light curves of images A and B of QJ 0158–4325 shifted by the time delay of  $\Delta t_{\rm A-B} = -14.5$  days estimated by Faure et al. (2009). The new X-ray data begin after epoch 6 (2010 October, JD–2450000 = 5476).

images) at >90% confidence, of which three iron lines are detected at >99% confidence. For the 10 *Chandra* observations of SDSS1004, we detect the iron line in eight out of the 40 spectra (10 epochs  $\times$  4 images) at >90% confidence, of which six iron lines are detected at >99% confidence. For several closely separated observations, we detect energy shifts of the Fe K $\alpha$  line in consecutive and closely separated epochs most likely produced by the same caustic crossing. For example, Figure 6 shows a likely caustic crossing in QJ0158 during 2013 December.

In Figure 8 we show the generalized Doppler shift parameter g of the Fe line as a function of the equivalent width (EW) of the iron line in RXJ1131. We find a correlation between g and the EW with a Kendall's rank correlation coefficient of

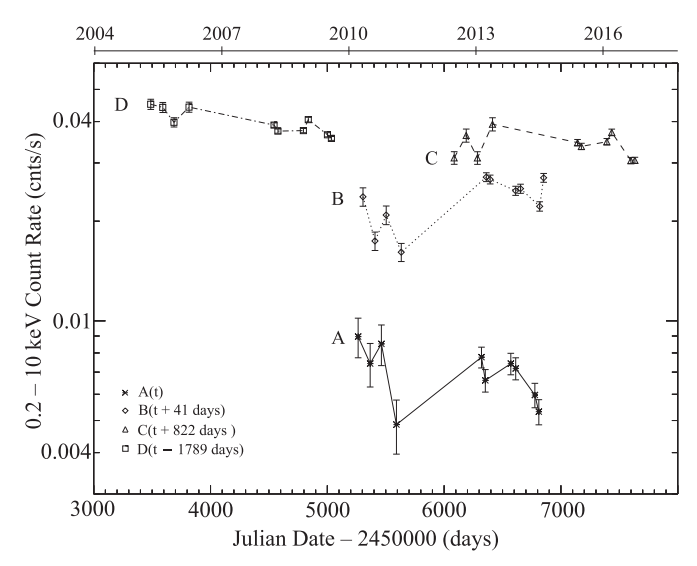


**Figure 3.** Total (0.2-10 keV) light curves of images A, B, C, and D of SDSS 1004+4112 shifted by the time delays estimated by Fohlmeister et al. (2008, 2016). We have added offsets of  $0.01 \text{ counts s}^{-1}$ ,  $0.02 \text{ counts s}^{-1}$ , and  $0.03 \text{ counts s}^{-1}$  to the light curves of the images B, C, and D, respectively, for clarity. The new X-ray data begin after epoch 5 (2013 March, JD-2450000 = 6353).

au=0.28 significant at >99.9% confidence. One possible explanation of this correlation is that blueshifted line emission is Doppler boosted, resulting in the observed EWs of the blueshifted lines being larger than the redshifted lines.

In Figure 9 we show the flux of the Fe line as a function of the flux of the continuum, where the line flux is the normalization of the Gaussian line component of the best-fit model, and the continuum flux is the normalization of the power-law component of the best-fit model calculated at 1 keV. We find a strong correlation between the line and continuum fluxes, with a Kendall's rank correlation coefficient of  $\tau = 0.5$ that is significant at >99.9% confidence. The flux of the X-ray continuum relative to the Fe K $\alpha$  line flux depends on a variety of accretion disk parameters and geometries, including the emissivity profile of the disk, the distance of the caustic from the black hole, the geometry of the corona, the geometry of the disk emission, the caustic crossing angle, and the inclination angle. Variations of the X-ray continuum and the Fe K $\alpha$  line flux during caustic crossing have been simulated in Popović et al. (2006) for a variety of accretion disk parameters and geometries. These simulations indicate that once the magnification caustic has passed over the black hole, the microlensing magnifications of the line and continuum regions are similar, and both the line and continuum decay in a similar manner with distance from the black hole. This may explain part of the observed correlation between these quantities.

## 3. The g and $\Delta E$ Distributions

We have recently developed a new technique based on microlensing that provides a robust constraint on the disk inclination angle and on the location of the ISCO, which in turn may provide an estimate of the spin of the black hole. Our technique is very simple. The stars near each lensed image produce magnification patterns with a characteristic Einstein

ID <sup>a</sup>	I.e. b	E C		-		At g			a - ci	P <sup>j</sup>	F <sup>k</sup>	n 1
ID <sup>a</sup>	Im <sup>b</sup>	$E_{\rm Fe}^{\ \ c}$ (keV)	$\sigma_{\mathrm{Fe}}^{}}^{}}$ (keV)	EW <sub>Fe</sub> <sup>e</sup> (keV)	$N_{ m Fe}^{ m \ f}$	$N_{\rm cont}^{}$	Γ	cstat <sup>n</sup>	dof	P	F"	$P_F^{-1}$
4814	1	$3.96^{+0.13}_{-0.14}$	$0.15^{+0.13}_{-0.15}$	$1.66^{+0.46}_{-0.97}$	$4.5^{+3.3}_{-2.6}$	$7.3^{+1.5}_{-1.3}$	$1.48^{+0.19}_{-0.19}$	118.44	163	1	6.41	< 0.001
4814	2	$2.60^{+0.05}_{-0.05}$	< 0.12	$0.26^{+0.06}_{-0.09}$	$9.6^{+4.8}_{-4.8}$	$46.7^{+3.3}_{-3.1}$	$1.35^{+0.06}_{-0.06}$	491.61	491	1	3.94	0.013
6912	2	$3.46^{+0.09}_{-0.25}$	< 0.25	$0.35^{+0.25}_{-0.19}$	$4.6^{+5.0}_{-3.6}$	$47.0^{+5.7}_{-5.2}$	$1.76^{+0.12}_{-0.12}$	217.63	264	1	2.57	0.033
6913	1	$2.94^{+0.05}_{-0.27}$	$0.03^{+0.53}_{-0.03}$	$0.61^{+0.37}_{-0.36}$	$4.2^{+6.5}_{-3.2}$	$18.8^{+3.9}_{-3.4}$	$1.76^{+0.20}_{-0.20}$	116.63	152	1	4.35	0.003
6913	1	$3.81^{+0.20}_{-0.52}$	< 0.12	$1.11_{-0.66}^{+0.73}$	$4.7_{-4.0}^{+6.0}$	$18.8^{+3.9}_{-3.4}$	$1.76^{+0.20}_{-0.20}$	116.63	152	1	4.34	0.004
6913	4	$2.42^{+0.04}_{-0.04}$	< 0.15	$1.01^{+0.53}_{-0.48}$	$3.5^{+3.3}_{-2.2}$	$6.7^{+2.1}_{-1.7}$	$1.76^{+0.29}_{-0.29}$	52.03	77	0	7.81	< 0.001
6914	1	$4.59^{+0.44}_{-0.65}$	$0.45^{+1.13}_{-0.45}$	$2.52^{+1.62}_{-1.44}$	$12.4^{+9.3}_{-8.0}$	$23.6^{+4.2}_{-3.7}$	$1.66^{+0.17}_{-0.17}$	146.05	191	1	2.99	0.03
6914	2	$2.77^{+0.07}_{-0.06}$	$0.01^{+0.17}_{-0.01}$	$0.73^{+0.20}_{-0.31}$	$9.4^{+10.2}_{-4.4}$	$33.7^{+4.7}_{-4.2}$	$1.81^{+0.14}_{-0.14}$	175.40	234	0	11.96	< 0.001
6914	4	$3.63^{+0.68}_{-0.67}$	< 0.60	$1.00^{+1.00}_{-0.60}$	$2.1^{+2.7}_{-1.6}$	$9.1^{+2.5}_{-2.1}$	$1.83^{+0.27}_{-0.26}$	92.55	95	1	2.24	0.1
6915	1	$2.59^{+0.11}_{-0.15}$	$0.22^{+0.17}_{-0.16}$	$0.59^{+0.19}_{-0.17}$	$48.4^{+20.3}_{-18.9}$	$144.0^{+9.7}_{-9.2}$	$1.62^{+0.06}_{-0.06}$	445.59	476	0	7.43	< 0.001
6915	1	$4.35^{+0.10}_{-0.10}$	$0.08^{+0.09}_{-0.08}$	$0.31^{+0.18}_{-0.16}$	$11.1^{+9.5}_{-7.9}$	$144.0^{+9.7}_{-9.2}$	$1.62^{+0.06}_{-0.06}$	445.59	476	1	7.42	< 0.001
6915	2	$3.81^{+0.05}_{-0.03}$	< 0.07	$0.49^{+0.15}_{-0.38}$	$8.1^{+5.5}_{-4.3}$	$91.6^{+7.7}_{-7.3}$	$1.91^{+0.09}_{-0.09}$	333.73	343	0	6.65	0.001
6916	1	$2.28^{+0.10}_{-0.06}$	< 0.30	$0.16^{+0.07}_{-0.05}$	$15.8^{+10.8}_{-10.5}$	$147.0^{+9.8}_{-9.3}$	$1.58^{+0.06}_{-0.07}$	440.07	479	1	4.30	0.001
6916	1	$2.95^{+0.09}_{-0.07}$	< 0.50	$0.24^{+0.09}_{-0.07}$	$16.2^{+10.5}_{-10.5}$	$147.0^{+9.8}_{-9.3}$	$1.58^{+0.06}_{-0.07}$	440.07	479	1	4.36	0.002
7785	2	$2.69^{+0.03}_{-0.03}$	< 0.10	$0.48^{+0.14}_{-0.11}$	$12.8^{+7.0}_{-5.8}$	$72.0^{+6.7}_{-6.3}$	$1.86^{+0.10}_{-0.10}$	295.14	312	0	9.40	< 0.001
7785	2 2	$3.18^{+0.05}_{-0.28}$	<0.10	$0.35^{+0.15}_{-0.21}$	$7.0^{+5.6}_{-4.4}$	$72.0^{+6.7}_{-6.3}$	$1.86^{+0.10}_{-0.10}$	295.14	312	1	9.40	< 0.001
7786 7787		$3.42^{+0.15}_{-0.09}$	$< 0.20$ $0.15^{+0.25}_{-0.15}$	$0.35_{-0.19}^{+0.15} \\ 0.24_{-0.16}^{+0.15}$	$9.7^{+9.7}_{-6.6}$	$89.0_{-6.7}^{+7.1} \\ 142.0_{-9.0}^{+9.5}$	$1.70_{-0.08}^{+0.08} \\ 1.74_{-0.07}^{+0.07}$	331.99 421.39	384	1	4.64	0.003 0.023
7787	1 1	$3.07^{+0.28}_{-0.23}$ $4.20^{+0.04}_{-0.05}$		$0.24_{-0.16}$ $0.32_{-0.14}^{+0.20}$	$12.0_{-11.4}^{+13.4} \\ 9.4_{-5.5}^{+6.8}$	$142.0_{-9.0}$ $142.0_{-9.0}^{+9.5}$	$1.74_{-0.07}$ $1.74_{-0.07}^{+0.07}$	421.39	439 439	1	4.10	0.023
7788	1	$3.92^{+0.30}_{-0.23}$	<0.08 <1.10	$0.32_{-0.14}$ $0.21_{-0.11}^{+0.10}$	$9.4_{-5.5}$ $13.6_{-5.4}^{+6.9}$	$142.0_{-9.0}$ $136.0_{-9.0}^{+9.4}$	$1.74_{-0.07}^{+0.07}$ $1.72_{-0.07}^{+0.07}$	362.37	423	1	4.10 2.46	0.012
7789	1	$2.49^{+0.08}_{-0.07}$	<0.40	$0.21_{-0.11}$ $0.17_{-0.09}^{+0.07}$	$13.0_{-5.4}^{+8.6}$ $11.4_{-7.4}^{+8.6}$	$136.0_{-9.0}$ $146.0_{-9.3}^{+9.7}$	$1.72_{-0.07}$ $1.82_{-0.07}^{+0.07}$	330.18	429	1	2.40	0.033
7789	2	$2.49_{-0.07}$ $2.87_{-0.04}^{+0.05}$	< 0.40	$0.17_{-0.09}$ $0.34_{-0.15}^{+0.12}$	$9.6^{+6.6}_{-5.3}$	$69.8_{-6.1}^{+6.5}$	$1.73^{+0.09}_{-0.09}$	300.18	339	0	4.97	0.006
7790	3	$2.42^{+0.20}_{-0.20}$	$0.24^{+0.21}_{-0.24}$	$1.04^{+0.36}_{-0.44}$	$13.0^{+9.6}_{-8.1}$	$21.7^{+3.7}_{-3.3}$	$1.69^{+0.16}_{-0.16}$	25.96	29	1	4.46	0.007
7791	2	$3.21^{+0.06}_{-0.05}$	< 0.10	$0.23^{+0.14}_{-0.13}$	$5.82^{+5.65}_{-4.42}$	$99.6^{+8.0}_{-7.5}$	$1.89^{+0.08}_{-0.08}$	294.67	340	1	2.08	0.04
7792	1	$2.55^{+0.07}_{-0.06}$	< 0.50	$0.20^{+0.10}_{-0.09}$	$11.3^{+9.1}_{-7.6}$	$145.0^{+10.0}_{-9.9}$	$1.92^{+0.08}_{-0.08}$	342.32	407	1	2.46	0.073
7792	2	$3.25^{+0.13}_{-0.12}$	$0.13^{+0.18}_{-0.13}$	$0.47^{+0.27}_{-0.21}$	$11.6^{+9.4}_{-7.6}$	$101.9^{+8.1}_{-7.7}$	$1.91^{+0.09}_{-0.08}$	333.74	363	1	2.81	0.1
7793	1	$3.75^{+0.05}_{-0.06}$	< 0.16	$0.22^{+0.12}_{-0.15}$	$6.7^{+6.3}_{-5.0}$	$122.9^{+8.9}_{-8.4}$	$1.75^{+0.07}_{-0.07}$	343.24	400	1	3.49	0.013
7793	2	$2.59^{+0.09}_{-0.07}$	$0.04^{+0.11}_{-0.04}$	$0.38^{+0.16}_{-0.22}$	$8.2^{+6.5}_{-6.0}$	$84.4^{+7.3}_{-6.9}$	$1.83^{+0.09}_{-0.09}$	312.71	346	1	2.44	0.023
7793	2	$4.97^{+0.09}_{-0.60}$	< 0.55	$0.46^{+0.31}_{-0.28}$	$4.9^{+13.4}_{-3.8}$	$84.4_{-6.9}^{+7.3}$	$1.83^{+0.09}_{-0.09}$	312.71	346	1	3.47	0.0033
7793	3	$2.63^{+0.05}_{-0.05}$	< 0.12	$0.91^{+0.48}_{-0.54}$	$3.1^{+3.4}_{-2.2}$	$7.1^{+2.2}_{-1.8}$	$1.73^{+0.29}_{-0.29}$	85.62	82	1	4.45	0.014
7794	2	$4.37^{+0.07}_{-0.07}$	< 0.75	$0.41^{+0.23}_{-0.17}$	$8.0^{+17.9}_{-5.7}$	$114.1^{+8.4}_{-8.0}$	$1.79^{+0.08}_{-0.07}$	375.19	401	1	4.10	0.0033
7794	3	$4.79^{+0.40}_{-0.39}$	< 0.14	$0.65^{+0.51}_{-0.40}$	$3.0^{+3.9}_{-2.5}$	$38.0^{+5.0}_{-4.6}$	$1.89^{+0.14}_{-0.13}$	166.94	221	1	3.76	0.01
9180	1	$2.81^{+0.07}_{-0.10}$	$0.05^{+0.43}_{-0.05}$	$0.11^{+0.04}_{-0.06}$	$5.8_{-4.2}^{+7.5}$	$101.6^{+4.5}_{-4.4}$	$1.62^{+0.04}_{-0.04}$	558.90	596	1	2.17	0.1
9180	3	$3.53^{+0.06}_{-0.07}$	< 0.17	$0.23^{+0.12}_{-0.14}$	$2.0_{-1.5}^{+1.9}$	$33.7^{+2.6}_{-2.5}$	$1.77^{+0.08}_{-0.08}$	368.30	385	1	2.60	0.02
9181	1	$2.35^{+0.10}_{-0.10}$	$0.15^{+0.11}_{-0.10}$	$0.20^{+0.06}_{-0.07}$	$18.2^{+10.7}_{-9.5}$	$142.1^{+5.4}_{-5.2}$	$1.65^{+0.04}_{-0.04}$	632.52	638	0	6.16	0.001
9181	1	$2.80^{+0.05}_{-0.05}$	< 0.12	$0.11^{+0.04}_{-0.06}$	$7.2^{+4.3}_{-4.3}$	$142.1^{+5.4}_{-5.2}$	$1.65^{+0.04}_{-0.04}$	632.52	638	1	6.14	0.001
9181	4	$3.70^{+0.05}_{-0.30}$	< 0.12	$0.59^{+0.36}_{-0.36}$	$1.5^{+1.3}_{-1.0}$	$12.0^{+1.6}_{-1.4}$	$1.84^{+0.13}_{-0.13}$	192.77	227	1	2.2	0.02
9237	2	$3.16^{+0.06}_{-0.05}$	< 0.13	$0.12^{+0.07}_{-0.06}$	$4.0^{+3.5}_{-2.8}$	$90.2^{+4.2}_{-4.0}$	$1.65^{+0.04}_{-0.04}$	560.80	584	1	2.07	0.037
9237	3	$3.84^{+0.06}_{-0.05}$	$0.05^{+0.08}_{-0.05}$	$0.59^{+0.19}_{-0.22}$	$3.8^{+2.4}_{-1.9}$	$30.7^{+2.5}_{-2.4}$	$1.81^{+0.08}_{-0.08}$	322.8	353	0	7.88	< 0.001
9237	4	$3.46^{+0.15}_{-0.28}$	$0.19_{-0.08}^{+0.32}$	$1.61^{+0.59}_{-0.60}$	$3.3^{+2.1}_{-1.7}$	$6.8^{+1.2}_{-1.1}$	$1.7^{+0.18}_{-0.17}$	183.75	195	0	5.56	< 0.001
9238	3	$2.72^{+0.10}_{-0.10}$	$0.13^{+0.13}_{-0.10}$	$0.72^{+0.27}_{-0.22}$	$5.8^{+3.7}_{-3.0}$	$21.4^{+2.2}_{-2.0}$	$1.85^{+0.10}_{-0.10}$	253.35	316	0	6.93	0.056
9238	3	$3.80^{+0.10}_{-0.09}$	$0.10^{+0.11}_{-0.10}$	$0.65^{+0.26}_{-0.29}$	$2.8^{+2.2}_{-1.8}$	$21.4^{+2.2}_{-2.0}$	$1.85^{+0.10}_{-0.10}$	253.35	316	0	2.88	0.033
9239	2	$2.41^{+0.07}_{-0.29}$	$0.05^{+0.28}_{-0.05}$	$0.13^{+0.07}_{-0.05}$	$4.9^{+8.0}_{-3.6}$	$63.5^{+3.5}_{-3.4}$	$1.65^{+0.05}_{-0.05}$	503.17	514	1	3.25	0.053
9240	2	$3.06^{+0.05}_{-0.29}$	< 0.10	$0.22^{+0.08}_{-0.07}$	$5.0^{+2.9}_{-2.9}$	$62.4^{+3.6}_{-3.6}$	$1.72^{+0.06}_{-0.06}$	498.60	495	1	2.97	0.046
9240	2	$3.96^{+0.17}_{-0.14}$	$0.20^{+0.24}_{-0.11}$	$0.55^{+0.24}_{-0.22}$	$8.1^{+7.5}_{-4.5}$	$62.4^{+3.6}_{-3.6}$	$1.72^{+0.06}_{-0.06}$	498.60	495	1	4.18	0.026
9240	4	$3.34^{+0.04}_{-0.04}$	< 0.06	$0.46^{+0.19}_{-0.18}$	$1.8^{+1.5}_{-1.1}$	$12.4^{+1.6}_{-1.5}$	$1.73^{+0.12}_{-0.12}$	228.56	260	1	3.75	0.063
11540	2	$3.27^{+0.04}_{-0.05}$	< 0.10	$0.09^{+0.04}_{-0.03}$	$3.2^{+2.2}_{-2.0}$	$91.4^{+3.1}_{-3.0}$	$1.63^{+0.03}_{-0.03}$	678.26	681	1	3.52	0.03
11540	2	$4.28^{+0.05}_{-0.05}$	<0.12	$0.16^{+0.23}_{-0.12}$	$3.4^{+2.0}_{-2.0}$	$91.4^{+3.1}_{-3.0}$	$1.63^{+0.03}_{-0.03}$	678.26	681	1	3.01	0.057
11540	3	$3.93^{+0.08}_{-0.16}$	$0.05^{+0.14}_{-0.05}$	$0.21^{+0.10}_{-0.15}$	$2.2^{+2.1}_{-1.6}$	$35.7^{+2.3}_{-2.1}$	$1.61^{+0.06}_{-0.06}$	411.79	496	1	2.69	0.02
11542	1	$2.36^{+0.05}_{-0.05}$	$0.13^{+0.06}_{-0.05}$	$0.22^{+0.04}_{-0.04}$	$3.0^{+9.9}_{-9.0}$	$149.7^{+4.1}_{-4.1}$	$1.39^{+0.02}_{-0.02}$	963.88	822	0	8.30	< 0.001
11542	1	$2.94^{+0.09}_{-0.09}$	$0.11^{+0.20}_{-0.07}$	$0.22^{+0.05}_{-0.04}$	$1.2^{+9.7}_{-6.3}$	$149.7^{+4.1}_{-4.1}$	$1.39^{+0.02}_{-0.02}$	963.88	822	0	2.63	0.01
11542	2	$3.18^{+0.03}_{-0.05}$	<0.10	$0.13^{+0.06}_{-0.05}$	$3.6^{+2.1}_{-2.1}$	$62.1^{+2.6}_{-2.6}$	$1.58^{+0.04}_{-0.04}$	633.02	641	1	2.82	0.02
11543	1 1	$2.31_{-0.04}^{+0.04} \\ 2.62_{-0.04}^{+0.04}$	<0.13 <0.07	$0.06^{+0.02}_{-0.03} \ 0.08^{+0.02}_{-0.02}$	$8.0^{+4.6}_{-4.6}$ $8.7^{+4.2}_{-4.1}$	$151.2_{-4.4}^{+4.4} \\ 151.2_{-4.4}^{+4.4}$	$1.44_{-0.03}^{+0.03} \\ 1.44_{-0.03}^{+0.03}$	233.51 233.51	184 184	1 0	2.56 4.79	0.01 0.01
11543 11543	3	$2.62_{-0.04}^{+0.05}$ $2.62_{-0.06}^{+0.05}$	< 0.07	$0.08_{-0.02}^{+0.02}$ $0.17_{-0.08}^{+0.11}$	$2.4^{+2.0}_{-1.7}$	$30.6^{+2.3}_{-2.2}$	$1.44_{-0.03}^{+0.07}$ $1.75_{-0.07}^{+0.07}$	255.51 354.98	408	1	2.66	0.01
11543	3	$4.30^{+0.04}_{-0.05}$	< 0.10	$0.17_{-0.08}$ $0.34_{-0.13}^{+0.14}$	$2.4_{-1.7}^{+1.6}$ $2.0_{-1.2}^{+1.6}$	$30.6_{-2.2}^{+2.3}$ $30.6_{-2.2}^{+2.3}$	$1.75_{-0.07}^{+0.07}$ $1.75_{-0.07}^{+0.07}$	354.98 354.98	408	1	2.00 1.91	0.06
11545	3	$3.83^{+0.05}_{-0.05}$	< 0.10	$0.34_{-0.13}$ $0.25_{-0.12}^{+0.13}$	$2.0_{-1.2}$ $2.3_{-1.4}^{+1.7}$	$35.6^{+2.5}_{-2.4}$	$1.73_{-0.07}$ $1.71_{-0.07}^{+0.07}$	334.98 104.89	130	1	3.72	0.003
11344	3	$3.63_{-0.05}$	<u></u> √0.∠0	$0.23_{-0.12}$	$2.3_{-1.4}$	$33.0_{-2.4}$	1./1_0.07	104.09	130	1	3.14	0.003

Table 5 (Continued)

ID <sup>a</sup>	Im <sup>b</sup>	E <sub>Fe</sub> c (keV)	σ <sub>Fe</sub> <sup>d</sup> (keV)	EW <sub>Fe</sub> e (keV)	$N_{ m Fe}^{ m \ f}$	$N_{\rm cont}^{\ \ g}$	Γ	cstat <sup>h</sup>	dof <sup>i</sup>	$P^{j}$	$\mathbf{F}^{\mathbf{k}}$	$P_F^{-1}$
11545	3	$2.96^{+0.06}_{-0.06}$	< 0.10	$0.28^{+0.12}_{-0.13}$	$2.1^{+1.7}_{-1.3}$	$20.2^{+2.0}_{-1.8}$	$1.75^{+0.09}_{-0.09}$	319.40	348	0	3.51	0.016
11545	3	$4.44^{+0.13}_{-0.14}$	$0.20^{+0.13}_{-0.14}$	$1.30^{+0.52}_{-0.46}$	$4.8^{+2.8}_{-2.3}$	$20.2^{+2.0}_{-1.8}$	$1.75^{+0.09}_{-0.09}$	319.40	348	0	6.09	0.004
12833	1	$3.97^{+0.04}_{-0.05}$	< 0.2	$0.21^{+0.07}_{-0.06}$	$6.4^{+3.6}_{-3.2}$	$121.5^{+5.5}_{-5.3}$	$1.69^{+0.04}_{-0.04}$	492.66	577	0	4.80	0.005
12833	2	$4.22^{+0.20}_{-0.33}$	$0.13^{+0.23}_{-0.13}$	$0.25^{+0.16}_{-0.13}$	$4.9_{-4.0}^{+5.0}$	$108.0^{+5.2}_{-5.0}$	$1.82^{+0.04}_{-0.04}$	497.50	542	1	2.93	0.037
12833	3	$4.84^{+0.12}_{-0.16}$	$0.1^{+0.24}_{-0.10}$	$0.74^{+0.33}_{-0.34}$	$4.0^{+3.8}_{-2.7}$	$40.7^{+3.8}_{-3.6}$	$1.84^{+0.09}_{-0.09}$	337.96	346	1	2.98	0.036
12834	2	$3.84^{+0.07}_{-0.08}$	$0.06^{+0.10}_{-0.06}$	$0.22^{+0.11}_{-0.11}$	$4.5^{+3.7}_{-3.0}$	$78.5^{+4.5}_{-4.3}$	$1.69^{+0.05}_{-0.05}$	496.96	522	1	3.58	0.023
12834	4	$4.42^{+0.05}_{-0.06}$	< 0.15	$0.66^{+0.46}_{-0.41}$	$1.0^{+1.2}_{-0.8}$	$9.0^{+1.6}_{-1.4}$	$1.82^{+0.16}_{-0.16}$	160.98	184	1	3.11	0.04
13962	1	$2.62^{+0.21}_{-0.28}$	< 0.80	$0.13^{+0.10}_{-0.10}$	$3.6^{+4.0}_{-3.3}$	$71.5^{+4.9}_{-4.6}$	$1.81^{+0.07}_{-0.07}$	423.80	454	1	5.10	0.001
13962	1	$3.91^{+0.30}_{-0.27}$	$0.38^{+0.28}_{-0.21}$	$0.80^{+0.43}_{-0.31}$	$11.5^{+8.5}_{-6.8}$	$71.5^{+4.9}_{-4.6}$	$1.81^{+0.07}_{-0.07}$	423.80	454	0	5.10	0.002
13962	3	$3.83^{+0.23}_{-0.18}$	$0.25^{+0.30}_{-0.20}$	$1.09^{+0.53}_{-0.28}$	$5.2^{+3.8}_{-2.9}$	$29.1^{+3.1}_{-2.8}$	$1.95^{+0.11}_{-0.11}$	267.15	324	0	3.97	0.003
13962	4	$3.90^{+0.07}_{-0.07}$	< 0.12	$0.38^{+0.20}_{-0.22}$	$1.4^{+1.5}_{-1.1}$	$20.1^{+2.4}_{-2.2}$	$1.87^{+0.11}_{-0.11}$	241.22	278	1	3.00	0.053
13963	1	$2.39_{-0.08}^{+0.07}$	$0.03^{+0.08}_{-0.03}$	$0.21^{+0.11}_{-0.11}$	$3.8^{+3.2}_{-2.9}$	$33.2^{+3.3}_{-3.2}$	$1.73^{+0.10}_{-0.10}$	401.43	403	1	4.32	0.007
13963	1	$3.29_{-0.06}^{+0.07}$	< 0.30	$0.22^{+0.07}_{-0.10}$	$2.8^{+2.4}_{-1.9}$	$33.2^{+3.3}_{-3.2}$	$1.73^{+0.10}_{-0.10}$	401.43	403	1	4.32	0.01
13963	2	$2.30^{+0.09}_{-0.09}$	$0.08^{+0.10}_{-0.08}$	$0.19^{+0.10}_{-0.11}$	$7.3^{+5.8}_{-4.6}$	$57.8^{+3.9}_{-3.7}$	$1.65^{+0.06}_{-0.06}$	463.75	506	1	3.94	0.0033
13963	2	$3.92^{+0.07}_{-0.06}$	$0.02^{+0.10}_{-0.02}$	$0.19^{+0.01}_{-0.01}$	$3.1^{+2.8}_{-2.2}$	$57.8^{+3.9}_{-3.7}$	$1.65^{+0.06}_{-0.06}$	463.75	506	1	3.95	0.001
13963	3	$2.42^{+0.10}_{-0.30}$	$0.04^{+0.40}_{-0.04}$	$0.23^{+0.15}_{-0.17}$	$2.2_{-1.8}^{+5.2}$	$15.8^{+2.1}_{-1.9}$	$1.68^{+0.12}_{-0.12}$	240.66	294	1	3.01	0.013
14507	1	$3.82^{+0.27}_{-0.27}$	< 0.14	$0.39^{+0.18}_{-0.19}$	$3.3^{+3.0}_{-2.2}$	$26.4_{-3.2}^{+3.6}$	$1.59^{+0.12}_{-0.12}$	268.03	282	1	3.28	0.03
14507	2	$3.60^{+0.05}_{-0.05}$	$0.05^{+0.08}_{-0.05}$	$0.54^{+0.20}_{-0.15}$	$6.7^{+4.2}_{-3.3}$	$42.9_{-4.0}^{+4.3}$	$1.70^{+0.09}_{-0.09}$	309.99	361	0	6.85	< 0.001
14507	3	$4.30^{+0.11}_{-0.29}$	$0.05^{+0.33}_{-0.05}$	$0.35^{+0.04}_{-0.03}$	$2.3^{+3.4}_{-1.7}$	$14.5^{+2.7}_{-2.3}$	$1.77^{+0.17}_{-0.16}$	150.66	198	1	3.93	0.002
14508	3	$4.24^{+0.23}_{-0.22}$	$0.30^{+1.00}_{-0.30}$	$1.59^{+0.80}_{-0.77}$	$6.2^{+4.1}_{-3.5}$	$19.4^{+3.0}_{-2.7}$	$1.74^{+0.14}_{-0.14}$	195.38	249	1	6.20	0.01
14510	4	$4.63^{+0.22}_{-0.21}$	$0.30^{+0.50}_{-0.10}$	$2.43^{+1.04}_{-1.11}$	$6.0^{+3.8}_{-3.2}$	$20.1^{+3.3}_{-2.9}$	$1.91^{+0.15}_{-0.15}$	46.62	61	1	6.81	< 0.001

radius of

$$R_{\rm E} = D_{\rm OS} \left[ \frac{4G \langle M \rangle}{c^2} \frac{D_{\rm LS}}{D_{\rm OL} D_{\rm OS}} \right]^{1/2},\tag{1}$$

where  $\langle M \rangle$  is the mean mass of the lensing stars, the  $D_{ij}$  are the angular diameter distances, and the subscripts L, S, and O refer to the lens, source, and observer, respectively.

These patterns contain caustic curves on which the magnification diverges. As the observer, lens, and source move, the quasar experiences a time-varying magnification whose amplitude is determined by the size of the source, with larger sources showing lower amplitudes because they more heavily smooth the magnification patterns (e.g., Wyithe et al. 2000, 2002; Kochanek 2004). If the X-ray emission is dominated by the inner edge of the disk, then the characteristic source size is  $r_{\rm s} \sim 10 r_{\rm g} \sim 10^{15} (M_{\rm BH}/10^9 \, M_{\odot})$  cm where  $r_{\rm g} = G M_{\rm BH}/c^2$ . The effective source velocity across the pattern for our three quasars is in the range  $v_{\rm e} \sim 600$ –785 km s<sup>-1</sup> (see Mosquera & Kochanek 2011), leading to two characteristic timescales for variability: the Einstein crossing time  $R_E/v_e$ , typically several

years, and the source crossing time  $r_s/v_e$ , typically a few months (see Table 4).

As a caustic crosses the accretion disk, it differentially magnifies the Fe  $K\alpha$  line emission to produce changes in the line profile. We will observe these as shifts in the line energy that we use to calculate the distribution of the fractional energy shifts  $g=E_{\rm obs}/E_{\rm rest}$  (the "g distribution"). We first present an analytic estimate of the energy shift of the iron line caused by microlensing and compare these analytic estimates with the observed energy shifts. Numerical simulations of microlensing events are presented later in the section. The observed energy,  $E_{\rm obs}$ , of a photon emitted near the event horizon of a supermassive black hole will be shifted with respect to the emitted rest-frame energy,  $E_{\rm emit}$ , due to general relativistic and Doppler effects. The ratio between the observed energy and the emitted rest-frame energy is often referred to as the generalized Doppler shift and is defined as

$$g = \frac{E_{\text{obs}}}{E_{\text{emit}}} = \delta \sqrt{\frac{\sum \Delta}{A}},$$
 (2)

<sup>&</sup>lt;sup>a</sup> Chandra Observation ID.

b Image numbers 1, 2, 3, and 4 correspond to images A, B, C, and D of RX J1131-1231.

<sup>&</sup>lt;sup>c</sup> Observed-frame energy of the shifted Fe line.

<sup>&</sup>lt;sup>d</sup> Observed-frame energy width of the shifted Fe line.

<sup>&</sup>lt;sup>e</sup> Rest-frame equivalent width of the shifted Fe line.

f Flux of the shifted Fe line in units of  $\times 10^{-6}$  photons cm<sup>-2</sup> s<sup>-1</sup>.

<sup>&</sup>lt;sup>g</sup> Flux density of the continuum in units of  $\times 10^{-5}$  photons keV<sup>-1</sup> cm<sup>-2</sup> s<sup>-1</sup> at 1 keV.

h Cash statistic.

i Degrees of freedom.

<sup>&</sup>lt;sup>j</sup> P values of 0 and 1 correspond to confidence detection levels of the shifted Fe line of >99% and >90%, respectively.

<sup>&</sup>lt;sup>k</sup> F statistic between the null and alternative model.

<sup>&</sup>lt;sup>1</sup> The probability of exceeding this F value as determined from the Monte Carlo simulations.

ID <sup>a</sup>	Im <sup>b</sup>	E <sub>Fe</sub> <sup>c</sup> (keV)	$\sigma_{\rm Fe}^{}$ (keV)	EW <sub>Fe</sub> <sup>e</sup> (keV)	$N_{\mathrm{Fe}}^{}}$	$N_{\rm cont}^{\rm g}$	Γ	cstat <sup>h</sup>	dof	$P^{j}$	F <sup>k</sup>	$P_F^{-1}$
14487	2	3.63 <sup>+0.04</sup> <sub>-0.04</sub>	0.01 <sup>+0.20</sup> <sub>-0.01</sub>	1.14 <sup>+0.70</sup> <sub>-0.62</sub>	$2.1_{-1.6}^{+2.4}$	$2.2^{+0.4}_{-0.3}$	1.94 <sup>+0.23</sup> <sub>-0.23</sub>	101.83	111	1	3.56	0.040
14487	1	$3.03_{-0.04}^{+0.21}$ $3.41_{-0.15}^{+0.21}$	$0.01_{-0.01}^{+0.60}$ $0.39_{-0.39}^{+0.60}$	$1.14_{-0.62}$ $2.25_{-0.73}^{+0.98}$	$7.1^{+4.3}_{-3.4}$	$4.8^{+0.5}_{-0.5}$	$1.94_{-0.23}^{+0.16}$ $1.92_{-0.15}^{+0.16}$	101.83	170	0	9.43	< 0.040
14485	1	$2.93^{+0.06}_{-0.06}$	$0.14^{+0.14}_{-0.14}$	$1.01^{+0.36}_{-0.40}$	$6.8^{+4.6}_{-3.7}$	$6.7^{+0.6}_{-0.6}$	$2.19_{-0.16}^{+0.17}$	166.84	191	0	6.50	< 0.001
14485	1	$4.37^{+0.57}_{-0.35}$	$1.10^{+1.50}_{-0.60}$	$3.86^{+1.61}_{-1.51}$	$10.3^{+6.6}_{-5.8}$	$6.7^{+0.6}_{-0.6}$	$2.19_{-0.16}^{+0.17}$	166.84	191	0	6.50	< 0.001
14484	1	$2.86^{+0.06}_{-0.06}$	< 1.9	$0.63^{+0.61}_{-0.49}$	$3.0^{+2.6}_{-1.9}$	$3.6^{+0.4}_{-0.3}$	$1.97^{+0.15}_{-0.15}$	152.69	168	1	3.92	0.023
14484	2	$2.83^{+0.13}_{-0.26}$	$0.3^{+1.1}_{-0.3}$	$2.21^{+1.24}_{-1.06}$	$4.2^{+3.6}_{-2.7}$	$1.3^{+0.3}_{-0.2}$	$1.92^{+0.30}_{-0.29}$	68.33	80	1	4.92	0.006
11561	1	$2.27^{+0.39}_{-0.35}$	$0.4^{+0.8}_{-0.4}$	$2.19^{+1.12}_{-0.96}$	$14.8^{+11.9}_{-9.4}$	$4.2^{+0.7}_{-0.6}$	$2.26^{+0.30}_{-0.28}$	55.67	81	1	6.63	0.003
11561	2	$2.84^{+0.31}_{-0.31}$	$0.5^{+1.3}_{-0.4}$	$4.41^{+2.63}_{-2.36}$	$10.5^{+10.9}_{-8.2}$	$2.2^{+0.6}_{-0.5}$	$2.13^{+0.45}_{-0.50}$	30.53	41	1	2.91	0.037
11560	1	$1.59^{+0.06}_{-0.06}$	$0.12^{+0.30}_{-0.12}$	$0.58^{+0.26}_{-0.24}$	$11.7^{+8.6}_{-7.0}$	$4.7^{+0.8}_{-0.7}$	$1.81^{+0.23}_{-0.23}$	106.62	105	1	4.72	0.005
11557	1	$1.73^{+0.04}_{-0.03}$	$0.01^{+0.13}_{-0.01}$	$0.55^{+0.28}_{-0.25}$	$10.4^{+8.7}_{-6.6}$	$5.5^{+0.9}_{-0.8}$	$1.94^{+0.26}_{-0.25}$	76.04	88	1	5.07	0.008

where the Doppler factor  $\delta$  is

$$\delta = \frac{\sqrt{1 - v_{\phi}^2}}{1 - v_{\phi} \cos \theta_c},\tag{3}$$

 $A=(r^2+a^2)^2-a^2\Delta\sin^2\theta,~\Sigma=r^2+a^2\sin^2\theta,~\Delta=r^2-2r_gr+a^2,$  and  $\theta_c$  is the angle between the direction of the orbital velocity  $v_\phi$  of the emitting plasma and our line of sight, neglecting the general relativistic effect of the bending of the photon trajectories and relativistic aberration (see appendix for details). In Section 4 we compare our analytic estimate of the generalized Doppler factor g with the observed limits of the g distributions of RXJ1131.

We next use numerical simulations to evaluate if the microlensing of the X-ray emission from a mass-accreting supermassive black hole can indeed produce energy spectra similar to the observed ones. The simulations assume that RXJ1131 accretes through a standard geometrically thin, optically thick accretion disk (Novikov & Thorne 1973; Shakura & Sunyaev 1973) described by the analytical general relativistic equations of Page & Thorne (1974). This assumption seems to be well justified for two reasons. Sluse et al. (2012) estimate that the black hole of RXJ1131 has a mass  $M_{\rm BH}$  between  $8 \times 10^7 \, M_{\odot}$  and  $2 \times 10^8 \, M_{\odot}$  and a bolometric luminosity of  $L_{\rm Bol} \approx 10^{45} \, {\rm erg \, s^{-1}}$ . The inferred ratio of  $L_{\rm Bol}/L_{\rm Edd}$  is therefore expected to range between 0.01 and 0.42. It is therefore likely that RXJ1131 is accreting in the regime in which accretion is believed to be dominated by a geometrically thin, optically thick accretion disk (see, e.g., the discussion in McKinney et al. 2014). General relativistic (radiation) magnetohydrodynamic simulations indicate that the analytical equations describe accretion disks reasonably accurately (Kulkarni et al. 2011; Noble et al. 2011; Penna

et al. 2012; Sądowski 2016). However, optical and UV observations of microlensing events in quasars indicate that accretion disks are larger than predicted by thin-disk theory (Morgan et al. 2010), and similar discrepancies are found using measurements of continuum lags in the nearby Seyferts NGC2617 (Shappee et al. 2014) and NGC5548 (Edelson et al. 2015; Fausnaugh et al. 2016).

We use a general relativistic ray-tracing code (Krawczynski 2012; Beheshtipour et al. 2016; Hoormann et al. 2016) to track photons of initially unspecified energy from a lamppost corona (Matt et al. 1991) to the observer, accounting for the possibility that the photons impinge on the accretion disk and either reflect or prompt the emission of Fe K $\alpha$  photons. The compactness of the corona has been observationally and independently confirmed via microlensing (e.g., Pooley et al. 2007; Morgan et al. 2008, 2012; Chartas et al. 2009, 2016; Dai et al. 2010; Mosquera et al. 2013; Blackburne et al. 2014, 2015; MacLeod et al. 2015) and reverberation studies (Fabian et al. 2009; de Marco et al. 2011; Kara et al. 2013, 2014, 2016; Cackett et al. 2014; Emmanoulopoulos et al. 2014; Uttley et al. 2014). The reverberation studies in many cases constrain the distance between the corona and central black hole to lie in the range of  $3-10r_{o}$ .

In our simulations, the corona is located above the black hole at a radial Boyer–Lindquist (BL) coordinate r=5  $r_{\rm g}$  slightly offset from the polar axis ( $\theta=10^{\circ}$ ) and emits isotropically in its rest frame. The zero component of the wave vector  $k^{\mu}$  of the photon packet is proportional to the energies of the photons, and we assume that the corona emits a power-law SED with a photon number power law of  $dN/dE \propto E^{-\Gamma}$  with  $\Gamma=1.75$ . After transforming the photon packet's wave vector into the global BL coordinates, the code integrates the geodesic equation until the photon packet either comes too close to the black hole horizon (when we assume it will enter the black

<sup>&</sup>lt;sup>a</sup> Chandra Observation ID.

<sup>&</sup>lt;sup>b</sup> Image numbers 1 and 2 correspond to images A and B of QJ 0158-4325.

<sup>&</sup>lt;sup>c</sup> Observed-frame energy of the shifted Fe line.

<sup>&</sup>lt;sup>d</sup> Observed-frame energy width of the shifted Fe line.

<sup>&</sup>lt;sup>e</sup> Rest-frame equivalent width of the shifted Fe line.

f Flux of the shifted Fe line in units of  $\times 10^{-6}$  photons cm<sup>-2</sup> s<sup>-1</sup>.

<sup>&</sup>lt;sup>g</sup> Flux density of the continuum in units of  $\times 10^{-5}$  photons keV<sup>-1</sup> cm<sup>-2</sup> s<sup>-1</sup> at 1 keV.

<sup>&</sup>lt;sup>h</sup> Cash statistic.

<sup>&</sup>lt;sup>1</sup> Degrees of freedom.

 $<sup>^{\</sup>rm j}$  P values of 0 and 1 correspond to confidence detection levels of the shifted Fe line of >99% and >90%, respectively.

 $<sup>^{\</sup>mathbf{k}}$  F statistic between the null and alternative model.

<sup>&</sup>lt;sup>1</sup> The probability of exceeding this F value as determined from the Monte Carlo simulations.

Table 7
Properties of Shifted Fe  $K\alpha$  Line and Continuum in SDSS 1004+4112

ID <sup>a</sup>	Im <sup>b</sup>	E <sub>Fe</sub> <sup>c</sup> (keV)	$\sigma_{\rm Fe}^{}$ (keV)	EW <sub>Fe</sub> e (keV)	$N_{\mathrm{Fe}}^{}}$	$N_{\rm cont}^{\rm g}$	Γ	cstat <sup>h</sup>	dof <sup>h</sup>	$P^{j}$	$F^k$	$P_F^{-1}$
11549	4	1.18+0.04	<0.1	0.60 <sup>+0.27</sup> <sub>-0.25</sub>	$3.6^{+2.8}_{-2.2}$	10.8+5.6	1.59 <sup>+0.28</sup> <sub>-0.29</sub>	57.68	80	0	6.76	0.004
14495	2	$2.12^{+0.05}_{-0.21}$	< 0.16	$0.61^{+0.23}_{-0.31}$	$1.8^{+1.4}_{-1.1}$	$21.0^{+2.9}_{-3.5}$	$1.89^{+0.13}_{-0.13}$	152.36	185	0	6.03	0.003
14495	4	$2.33^{+0.14}_{-0.13}$	$0.30^{+0.13}_{-0.10}$	$4.36^{+1.30}_{-1.08}$	$4.4^{+1.8}_{-1.7}$	$15.3^{+4.7}_{-3.6}$	$2.17^{+0.23}_{-0.21}$	124.95	150	0	14.3	< 0.001
14496	2	$3.10^{+0.06}_{-0.07}$	< 0.12	$0.74^{+0.34}_{-0.34}$	$1.2^{+1.0}_{-0.8}$	$19.4^{+3.9}_{-3.3}$	$1.79_{-0.13}^{+0.13}$	185.30	200	1	4.12	0.02
14496	3	$2.36^{+0.07}_{-0.07}$	< 0.20	$1.71^{+0.60}_{-0.56}$	$2.8^{+1.5}_{-1.5}$	$16.5^{+5.1}_{-4.0}$	$1.93^{+0.21}_{-0.19}$	159.62	196	0	9.07	< 0.001
14498	1	$1.80^{+0.05}_{-0.36}$	< 0.37	$0.58^{+0.26}_{-0.24}$	$1.0^{+0.7}_{-0.6}$	$8.3^{+3.0}_{-2.2}$	$1.81^{+0.21}_{-0.21}$	94.73	124	0	7.59	< 0.001
14498	1	$2.23^{+0.05}_{-0.08}$	< 0.11	$1.02^{+0.51}_{-0.50}$	$1.2^{+1.0}_{-0.8}$	$8.3^{+3.0}_{-2.2}$	$1.81^{+0.21}_{-0.21}$	94.73	124	0	7.54	< 0.001
14500	2	$1.81^{+0.05}_{-0.04}$	< 0.10	$0.30^{+0.12}_{-0.12}$	$1.3^{+1.0}_{-0.8}$	$23.2_{-4.0}^{+4.8}$	$1.84^{+0.13}_{-0.13}$	178.21	204	1	4.59	0.008

<sup>&</sup>lt;sup>1</sup> The probability of exceeding this F value as determined from the Monte Carlo simulations.

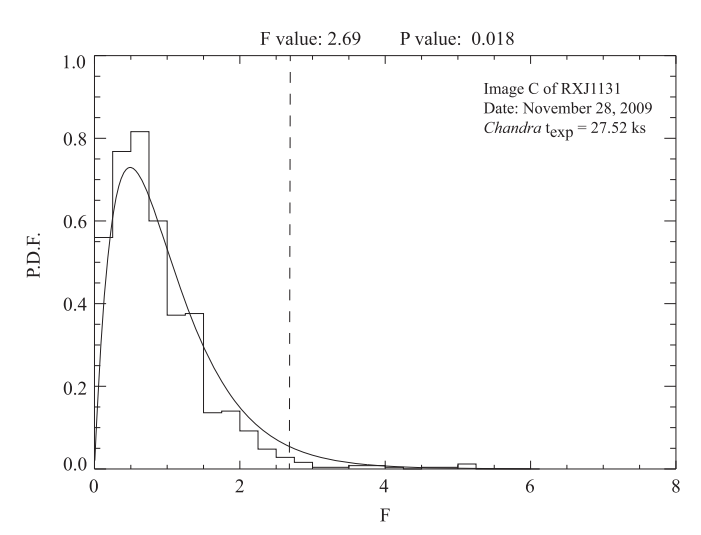


**Figure 4.** Monte Carlo simulated (histogram) and theoretical (smooth curve) probability density distributions of the F statistic between fits of models that included a simple absorbed power law (null model), and one that included one Gaussian emission line (alternative model) to the observed spectrum of image C of RXJ 1131 obtained in 2009 November 28 (obsid = 11540). We find that the probability of obtaining an F value larger than 2.69 is P = 0.018.

hole), impinges on the accretion disk, or arrives at a fiducial stationary observer at  $r_{\rm obs} = 10,000 \, r_{\rm g}$ .

We assume that the accretion disk extends from the ISCO to 100  $r_{\rm g}$ . We use simple prescriptions for treating the absorption, reflection, and reprocessing in the disk's photosphere. If a photon packet hits the disk, it is absorbed with probability  $p_{\rm abs}$ , it scatters with probability  $p_{\rm es} = (1-p_{\rm abs})R/(1+R)$ , or it prompts the emission of a monoenergetic Fe K $\alpha$  photon with probability  $p_{\rm Fe-K}\alpha = (1-p_{\rm abs})/(1+R)$ , so that  $p_{\rm es}/p_{\rm Fe-K}\alpha = R$ . Although we use  $p_{\rm abs} = 0.9$  and R = 1, the results do not depend strongly on the specific choice (see Ross & Fabian 2005; García et al. 2013, for more detailed

treatments). The Fe K $\alpha$  photons are always emitted with an energy of 6.4 keV in the rest frame of the accretion disk with a statistical weight that depends on the net redshift or blueshift g incurred between the emission of the photon in the corona and its absorption in the accretion disk. More specifically, the weight is given by  $w = g^{\Gamma-1}$  with

$$g = \frac{u_{\hat{\mu}}k^{\hat{\mu}}}{u_{\check{\mu}}k^{\check{\mu}}}. (4)$$

Here,  $u^{\mu}$  and  $u^{\mu}$  denote the four velocities of the corona and the accretion disk plasmas, respectively, and  $k^{\mu}$  and  $k^{\mu}$  denote the photon packet wave vectors in the rest frames of the corona plasma and accretion disk plasma (before the absorption of the photon packet), respectively. The scattering model is based on the classical treatment by Chandrasekhar (1960) of scattering by an indefinitely deep electron atmosphere. Tracking photon packets forward in time allows us to model multiple interactions of the photon packets with the accretion disk before or after a photon packet prompts the emission of a Fe K $\alpha$  photon packet (see also Schnittman & Krolik 2009, 2010, and references therein). Our treatment neglects the possibility that Fe K $\alpha$  photons return to the accretion disk and may prompt the emission of another Fe K $\alpha$  photon, but this is a very small correction. When a photon packet reaches the observer, its wave vector is transformed from the global BL frame into the reference frame of a coordinate stationary observer. Although we simulated 10 million photon packets for a range of black hole spins (a = 0, 0.1, 0.2, ..., 0.9, 0.95, 0.98,0.998), we will show here only example results for a = 0.3. The results for other black hole spins will be presented in a forthcoming paper (H. Krawczynski et al. 2017, in preparation).

<sup>&</sup>lt;sup>a</sup> Chandra Observation ID.

<sup>&</sup>lt;sup>b</sup> Image numbers 1, 2, 3, and 4 correspond to images A, B, C, and D of SDSS 1004+4112.

<sup>&</sup>lt;sup>c</sup> Observed-frame energy of the shifted Fe line.

<sup>&</sup>lt;sup>d</sup> Observed-frame energy width of the shifted Fe line.

<sup>&</sup>lt;sup>e</sup> Rest-frame equivalent width of the shifted Fe line.

f Flux of the shifted Fe line in units of  $\times 10^{-6}$  photons cm<sup>-2</sup> s<sup>-1</sup>.

<sup>&</sup>lt;sup>g</sup> Flux density of the continuum in units of  $\times 10^{-5}$  photons keV<sup>-1</sup> cm<sup>-2</sup> s<sup>-1</sup> at 1 keV.

h Cash statistic

<sup>&</sup>lt;sup>1</sup> Degrees of freedom.

<sup>&</sup>lt;sup>j</sup> P values of 0 and 1 correspond to confidence detection levels of the shifted Fe line of >99% and >90%, respectively.

<sup>&</sup>lt;sup>k</sup> F statistic between the null and alternative model.

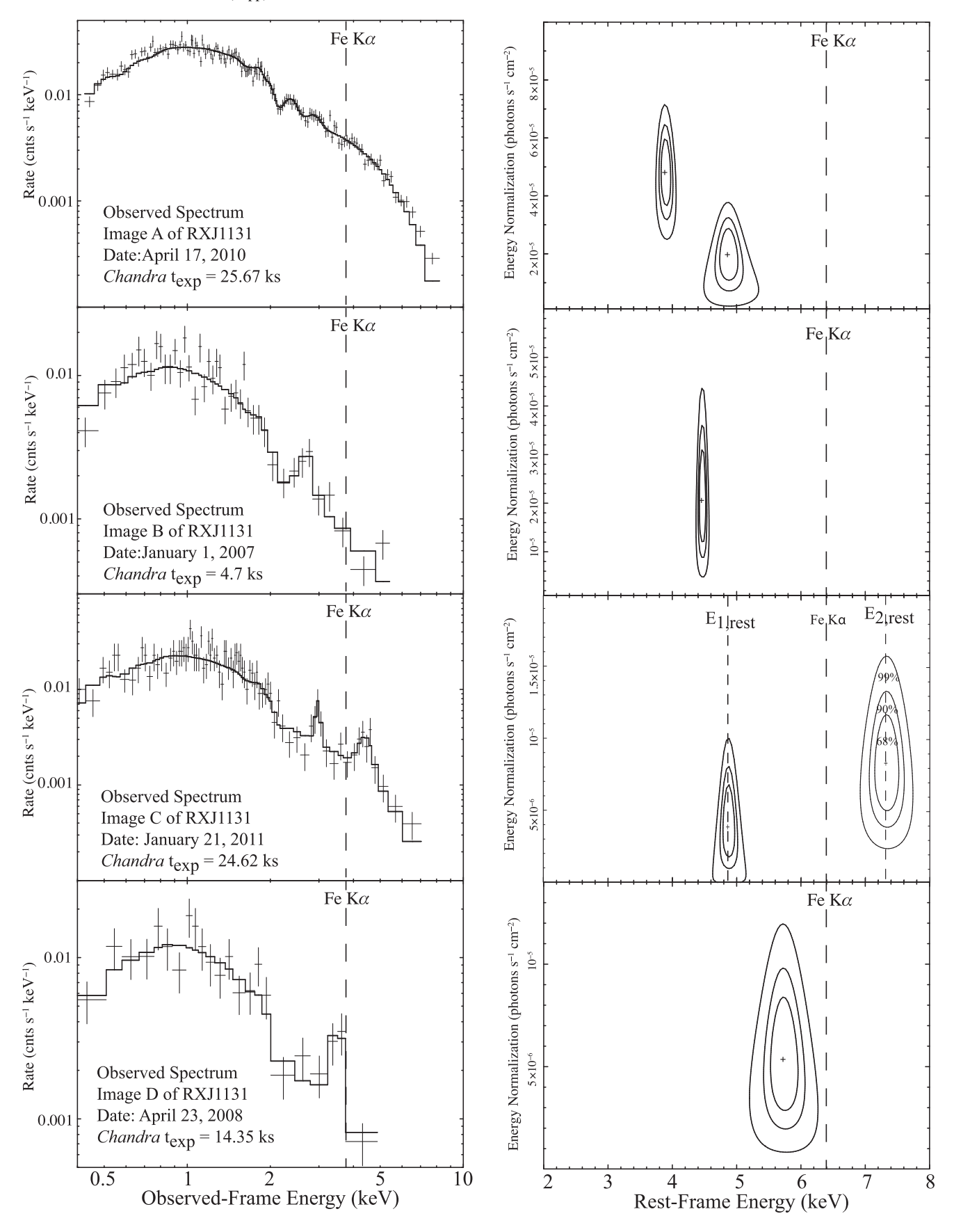


Figure 5. Left: spectra of images A, B, C, and D of RXJ1131 at four different epochs showing the shifted iron lines. The best-fit model is composed of a power law, one or two Gaussian lines, and Galactic and intrinsic absorption. Right: the 68%, 90%, and 99%  $\chi^2$  confidence contours for the line energies and flux normalizations.

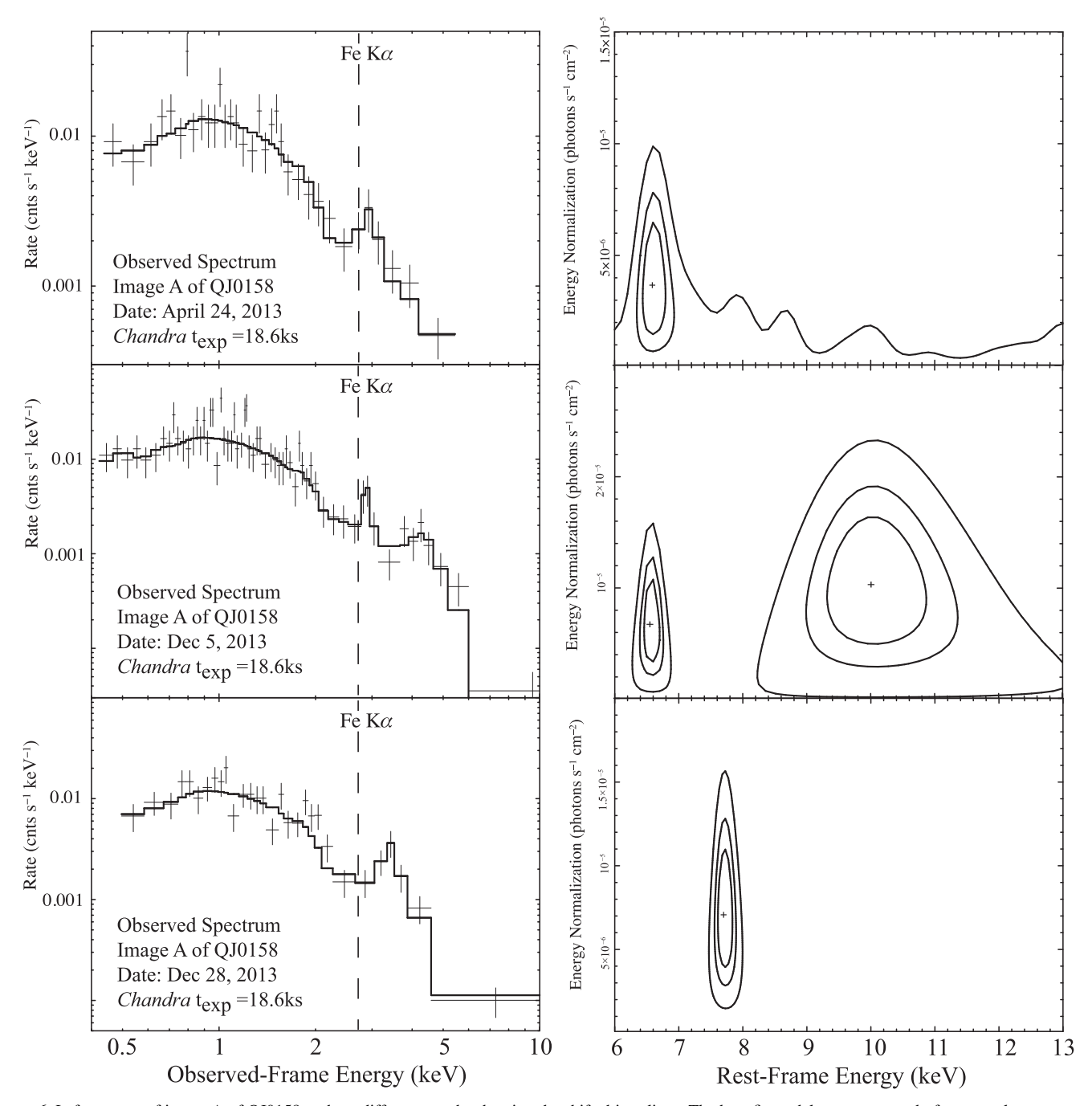


Figure 6. Left: spectra of image A of QJ0158 at three different epochs showing the shifted iron lines. The best-fit models are composed of a power law, one or two Gaussian lines, and Galactic and intrinsic absorption. Right: the 68%, 90%, and 99%  $\chi^2$  confidence contours for the line energies and flux normalizations.

In this paper we use the general parameterization of the microlensing magnification  $\mu$  close to caustic folds above the magnification  $\mu_0$  outside the caustic (see, e.g., Schneider et al. 1992; Chen et al. 2013):

$$\mu = 1 + \frac{K}{\mu_0 \sqrt{y_\perp}} H(y_\perp), \tag{5}$$

with  $y_{\perp}$  giving the position of the origin of the emission in the source plane along a coordinate axis perpendicular to the fold, K is the caustic amplification factor, and H is the Heaviside function (i.e.,  $H(y_{\perp}) = 0$  for  $y_{\perp} < 0$  and  $H(y_{\perp}) = 1$  for

 $y_{\perp} \geqslant 0$ ). For microlensing by a random field of stars,  $K/\mu_0$  is given by (Witt et al. 1993; Chartas et al. 2002)

$$K/\mu_0 \approx \beta \sqrt{\zeta_{\rm E}},$$
 (6)

where  $\beta$  is a constant of order unity, and  $\zeta_{\rm E}$  is the Einstein radius for stars of average mass  $\langle M \rangle$ . In this paper, we show results for  $\beta=0.5$  and  $\zeta_{\rm E}=1640\,r_{\rm g}$ , corresponding to  $\langle M \rangle=0.25\,M_{\odot}$  and  $M_{\rm BH}=10^8\,M_{\odot}$ . For each simulated black hole spin, we simulate caustic crossings at crossing angles  $\theta_c$  (the angle between the normal of the caustic fold and the black hole spin axis) between  $0^\circ$  and  $360^\circ$  in  $20^\circ$  steps and for  $-30\,r_{\rm g}$ 

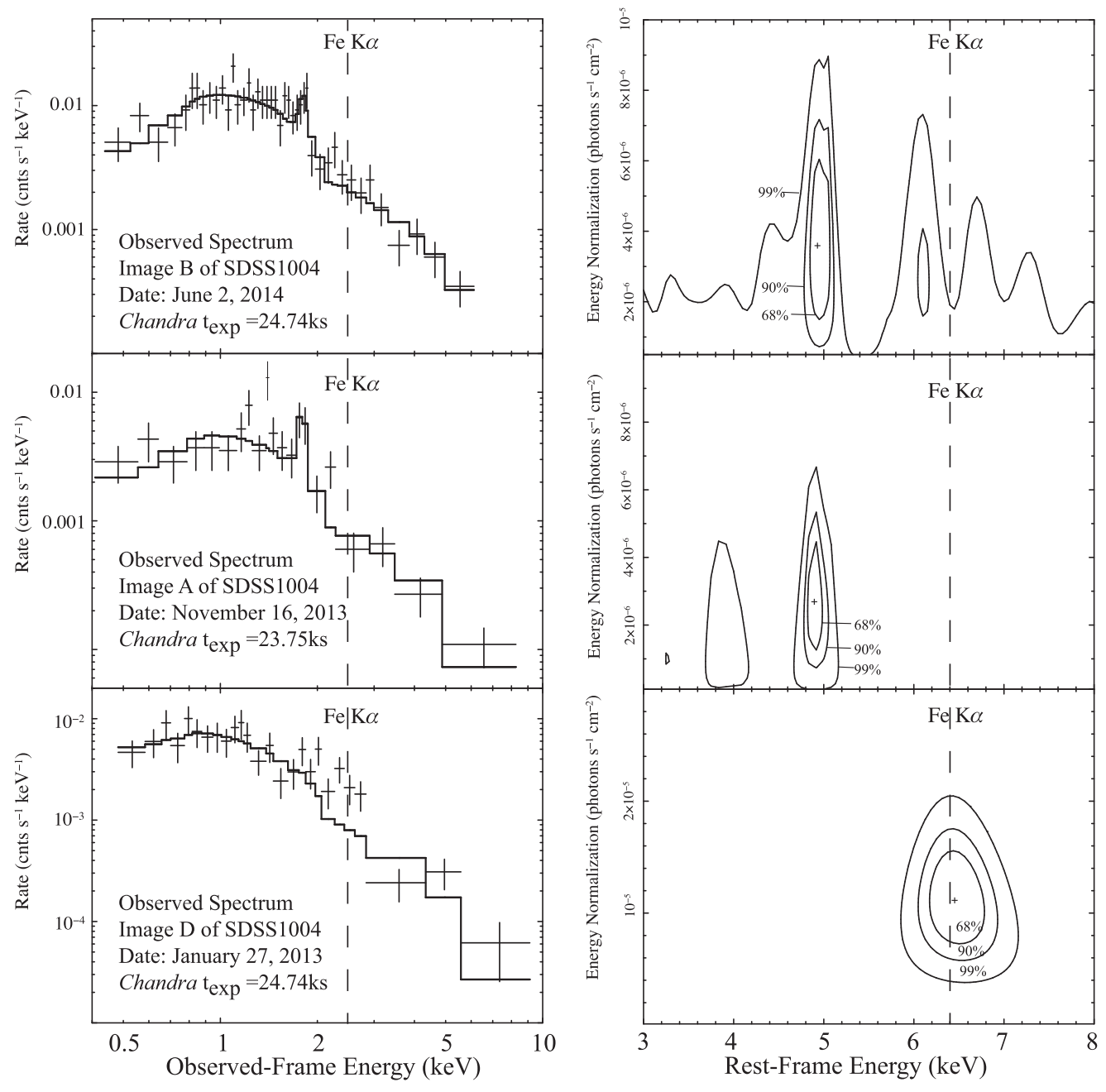


Figure 7. Left: spectra of images B, A, and D of SDSS1004 at three different epochs showing shifted iron lines. The best-fit models are composed of a power law, a Gaussian line, and Galactic and intrinsic absorption. The model for image D does not include the Gaussian line to better show the residual line emission near the instrumental edge at  $\sim$ 2 keV. Right: the 68%, 90%, and 99%  $\chi^2$  confidence contours for the line energies and flux normalizations.

to  $+30\,r_{\rm g}$  offsets of the caustic from the center of the black hole. An angle of  $\theta_c=0$  corresponds to a caustic fold perpendicular to the black hole spin axis with the positive side of the caustic (the side with  $\mu>1$ ) pointing in the  $\theta=0$  direction.

The left panel of Figure 10 shows a 2D map of the surface brightness of the Fe K $\alpha$  line emission in the source plane after convolving it with a caustic magnification ( $a=0.3, i=82^{\circ}.5, \theta_c=\pi/2$ ). An actual observer would see a different surface brightness distribution, as Figure 10 accounts for the flux magnification but not for the image distortion caused by the gravitational lensing. The magnification pattern of Equation (5) can clearly be recognized by a sudden jump from  $\mu=1$  to

 $\mu\gg 1$ , followed by the gradual return of the magnification to  $\mu\approx 1$ . The right panel shows the resulting Fe K $\alpha$  energy spectrum. Similar to the *Chandra* energy spectra shown in Figure 5, the simulated energy spectrum exhibits two distinct peaks. Scrutinizing similar maps and energy spectra for different caustic crossing angles and offsets reveals that double peaks appear naturally (but not only) when the positive side of the caustic magnifies lower surface brightness emission that is not as strongly Doppler boosted as the emission from the portions of the accretion disk approaching the observer with near-relativistic speed.

Figure 11 shows a 2D map of the g factors of the Fe K $\alpha$  photons for the same parameters as in Figure 10. The image

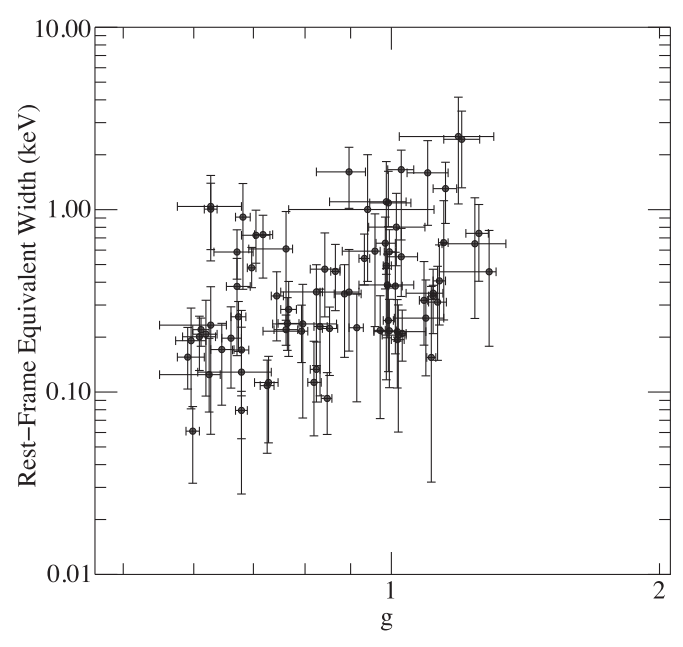


**Figure 8.** Fe line equivalent width as a function of the generalized Doppler shift parameter g for all images of RXJ1131. Only cases where the Fe line is detected at >90% confidence are shown.

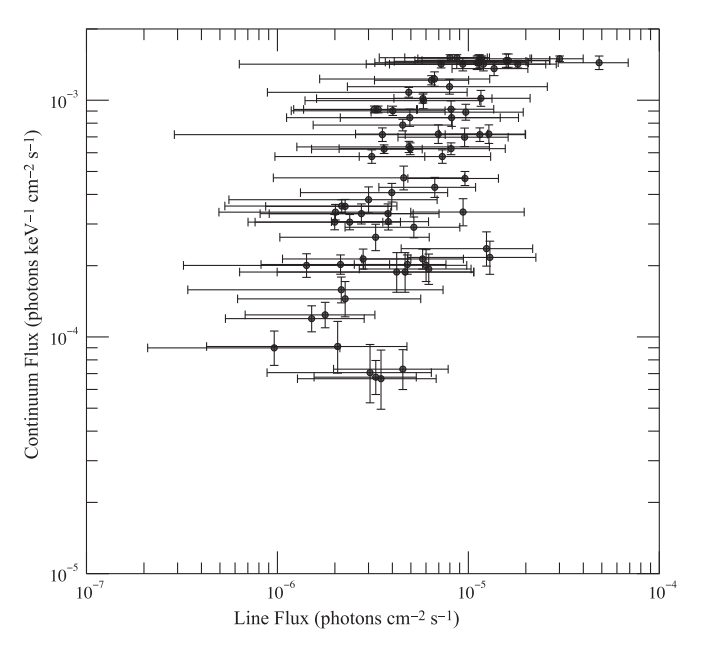


**Figure 9.** Flux of the Fe  $K\alpha$  line as a function of the continuum flux for Fe  $K\alpha$  lines detected at  $>\!90\%$  confidence in RXJ1131. The line flux is the normalization of the Gaussian line component of the best-fit model. The continuum flux is the normalization of the power-law component of the best-fit model calculated at 1 keV.

clearly shows the highest blueshifts from regions of the accretion disk moving toward us with near-relativistic speed.

Note that the gravitational redshift wins over the Doppler blueshift very close to the event horizon. The minimum and maximum g values are 0.42 and 1.4, respectively, and are in good agreement with the observed values. We have explored the dependence of the observed g values on the coronal height. We find that for larger coronal heights the g distribution

becomes narrower, as the inner edge of the disk is not illuminated as much as it is for low coronal heights, and thus the extreme g-factor emission is less intense. We conclude that for larger coronal heights the observed  $g_{\rm max}$  value for RXJ1131 would imply even higher inclinations.

We analyzed the energy spectra for all caustic crossing angles and offsets with an algorithm identifying the most prominent peaks and fitting them with Gaussians. The algorithm first finds the highest peak in the photon number energy spectrum (dN/dE) and then searches for an additional peak that rises more than 10% above the valley between the two peaks. Figure 12 shows the distribution of all the peak energies found in this way (singles and doubles). Figure 13 presents all simulated and observed double peak energies. Although a statistical analysis of the results is outside the scope of this paper, we will see in Section 4 that the simulated results do resemble the observed ones at least on a qualitative level.

#### 4. Results

We detect shifted and broadened Fe K $\alpha$  lines in almost every image of RXJ1131 that has an exposure time of >20 ks, as shown in Figure 5 and Table 5. Relativistically broadened Fe K $\alpha$  lines detected in the spectra of unlensed AGNs are produced from emission originating from the entire inner accretion disk. In contrast, the microlensed Fe  $K\alpha$  lines in the spectra of lensed AGNs are produced from a relatively smaller region on the disk that is magnified as a microlensing caustic crosses the disk. We therefore expect microlensed Fe K $\alpha$  lines to be in general narrower and with larger EWs than those detected in unlensed AGNs. The observed EWs of Fe K $\alpha$  lines in RXJ1131 are significantly affected by microlensing of both the direct continuum emission of the corona and the reflected line and continuum from the disk. The relative microlensing magnification of the direct and reflected emission was simulated in Popovic et al. (2006) for a variety of accretion disk parameters and geometries. Chen et al. (2012) compared the properties of a sample of lensed quasars with nonlensed ones and found that the EWs of the Fe lines detected in lensed quasars are systematically higher than those found in nonlensed ones, and this can be explained as the result of microlensing of both the continuum and line emission.

The presence of these energy shifts is evidence that most of the shifted iron line emission detected in RXJ1131 does not originate from reflection from a torus or other distant material but from material near the event horizon of the black hole. The evolution of the energy and shape of the Fe K $\alpha$  line during a caustic crossing depends on the ISCO, spin, inclination angle of the disk, and caustic angle. The extreme shifts are produced when the microlensing caustic is near the ISCO of the black hole. Measurements of the distribution of the fractional energy shifts  $g = E_{\rm obs}/E_{\rm rest}$  of the Fe K $\alpha$  line due to microlensing therefore provide a powerful limit on the g distribution that can be used to estimate the ISCO, spin, and inclination angle of the disk

In Figure 14 we show the g distribution (multiplied by the rest-frame energy of the Fe K $\alpha$  line,  $E_{\rm rest}=6.4\,{\rm keV})$  of the Fe K $\alpha$  lines with >90% and >99% detections in RXJ1131 for all images and epochs. One important feature of this iron line energy-shift distribution is the significant limits of the distribution at rest-frame energies of  $E_{\rm min}=3.78^{+0.16}_{-0.10}~{\rm keV}$  and  $E_{\rm max}=8.24^{-0.48}_{+0.15}~{\rm keV},$  where the error bars for both  $E_{\rm min}$  and  $E_{\rm max}$  are at the 90% confidence level, for iron lines detected

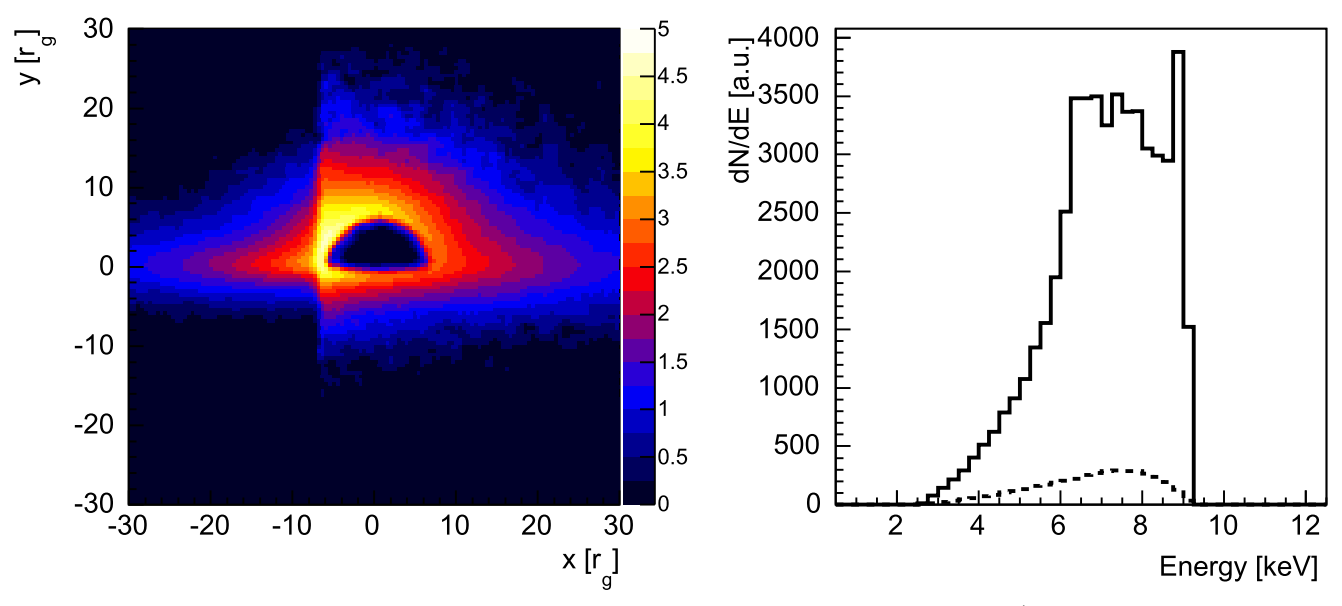


Figure 10. The left panel shows an image of the surface brightness of the Fe K $\alpha$  line emission as seen by an observer at  $10^4$   $r_{\rm g}$  and an inclination of  $i=82^\circ$ .5 from a black hole of spin a=0.3 for a caustic crossing angle of  $\theta_c=\pi/2$ . The surface brightness scale is logarithmic with an arbitrary absolute scale. The surface brightness exhibits a left-right asymmetry owing to the motion of the accretion disk plasma toward (left) or away from (right) the observer. The right panel shows the resulting energy spectrum of the Fe K $\alpha$  emission in the rest frame of the source.

at >90% confidence. These limits represent the most extremely redshifted and blueshifted Fe K $\alpha$  lines. If we interpret the largest energy shifts as being due to X-ray emission originating close to the ISCO, we obtain upper limits on the size of the ISCO and inclination angle of RXJ1131. In Figure 15 we show the g distribution for the individual images of RXJ1131. The apparent differences of the distributions between images can be a result of several factors, including the differences in the frequency of microlensing along different lines of sight, the differences in the S/N of the spectra (D being the faintest image), and differences in caustic crossing angles. The observed g distributions of Figures 14 and 15 closely resemble the simulated distribution of all peaks shown in Figure 12.

The energies of photons emitted from a ring at the ISCO are bounded by maximum and minimum values,  $g_{\text{max}}$  and  $g_{\text{min}}$ , of the generalized Doppler shift. The maximum blueshift of the Fe line places a constraint on the inclination angle. Specifically, for RXJ1131 the measured generalized Doppler factor  $g_{\rm max} = 1.29 \pm 0.04$  (90% confidence) constrains the inclination angle to be  $\gtrsim 64^{\circ}$ , for any values of the spin parameter and caustic crossing angle, as shown in Figure 16, assuming that the thin accretion disk extends all the way down to the ISCO. If we also require that the measured  $g_{\min}$  and  $g_{\max}$  shifts are produced by photons emitted from the same radius, then the inclination angle is required to be  $i \gtrsim 76^{\circ}$  for photons emitted from a radius of  $r \sim 8.5 r_g$  for any values of the spin parameter and caustic crossing angle, as also shown in Figure 16. We conclude that the current observed values of  $g_{\min}$  and  $g_{\max}$ place an upper limit on the ISCO radius of  $r_{\rm ISCO} \lesssim 8.5 r_{\rm g}$  and a disk inclination angle of  $i \gtrsim 76^{\circ}$ . If we only consider energy shifts detected above the 99% confidence level, the upper limit on the ISCO radius is  $r_{\rm ISCO} \lesssim 8.5 r_{\rm g}$  and the lower limit on the disk inclination angle is  $i \gtrsim 55^{\circ}$ .

The  $g_{\min}$  value provides an estimate of the radius of the emission region closest to the center of the black hole. If one assumes that the innermost emission region is near the ISCO radius, one can obtain a constraint on the spin of the black hole based on the relation between ISCO and spin. However, recent

3D MHD simulations of thin accretion disks indicate slight bleeding of the iron line emission to the region inside the ISCO (e.g., Reynolds & Begelman 1997). Reynolds & Fabian (2008) have attempted to estimate the systematic error on inferred black hole spin using the relativistic iron line method to infer the true spin of a black hole. They find that the systematic errors can be significant for slowly spinning black holes but become appreciably smaller as one considers more rapidly rotating black holes. In a future paper we plan to perform an analysis of the systematic errors on inferred black hole spin derived from the *g* distribution method and from the distribution of energy separations of double peaked lines caused by the possible bleeding of the iron line emission to the region inside the ISCO.

We also detect energy shifts in the Fe line in QJ0158 and SDSS1004, but they have not been monitored as frequently as RXJ1131. In Figure 17 we show the g distributions of the Fe K $\alpha$  lines with >90% confidence detections in QJ0158 and SDSS1004 for all images and epochs. These g distributions of QJ0158 and SDSS1004 are too sparsely populated to provide statistically significant constraints on the ISCO radii with the available data but demonstrate that these lenses also have microlensed Fe emission.

In several observations we detect two shifted Fe lines, as shown in Figures 6 and 7. Specifically, the numbers of detected double lines in the spectra of images A, B, C, and D of RXJ1131 are 9, 5, 3, and 0, respectively. All of the cases are detected at the >90% confidence level. In the following, we call energy spectra with one peak "singles" and energy spectra with two peaks "doubles." We searched for possible correlations between the energies of the doubles. A moderately significant correlation, with a Kendall's rank correlation coefficient of  $\tau = 0.6$  and a significance of >98% confidence, is detected between the observed  $E_{\rm min}$  and  $E_{\rm max}$  values in image A. The observed energies of the double lines detected in the spectra of image A and the spectra of all images are shown in Figures 18 and 19, respectively. We performed a straight-line least-squares fit to the data with the FITEXY routine (Press et al. 1992), which takes

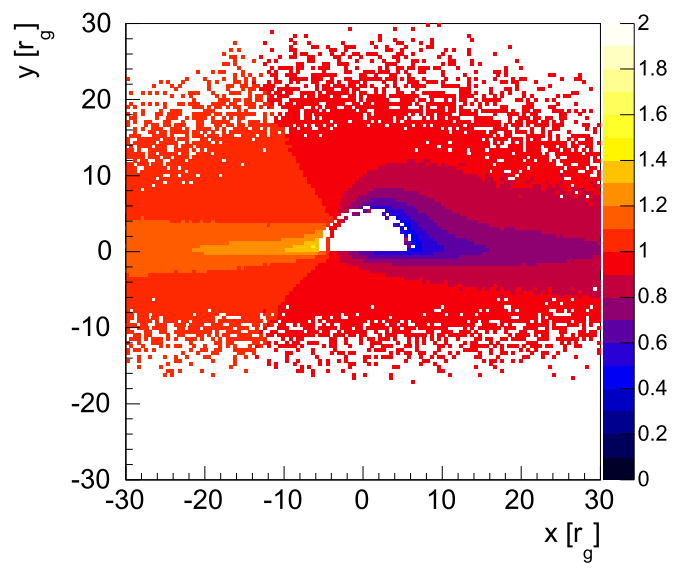


**Figure 11.** Map of the g factors of the Fe K $\alpha$  emission originating in the accretion disk. The net g factors result from the motion of the accretion disk plasma relative to the observer shown in Figure 9 and the propagation of the photon through the curved spacetime for the same parameters as were used in Figure 9.

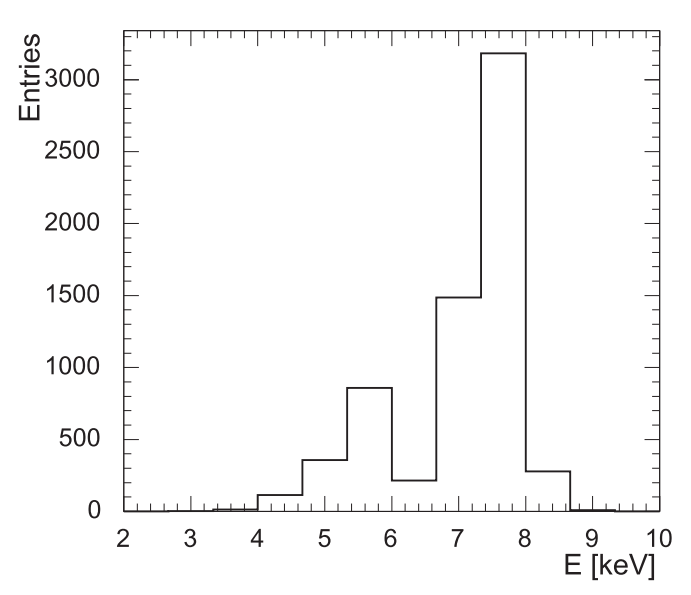


**Figure 12.** Simulated distribution of the single and double peak Fe line energies for a black hole with a spin of a=0.3 seen at an inclination of i=82.5.

into account errors in both coordinates. Based on the magnification maps of RX J1131–1231 (see Figures 4–6 of Dai et al. 2010), we expect a limited range of caustic crossing angles over  $\sim$ 10 years. Any change in the caustic crossing angle over time will contribute to the scatter in the observed  $E_{\rm min}$  and  $E_{\rm max}$  values of doubles. The scatter in the  $E_{\rm min}$  and  $E_{\rm max}$  values detected in all images is even larger, as we would expect from the differences in the caustic structures and their directions of motion in different images (Kendall's  $\tau=0.4$ , significant at >97% confidence).

In Figure 20 we show the  $\Delta E$  distribution of the rest-frame energy separations for the Fe line pairs detected in all images of RXJ1131 at the >90% confidence level, where  $\Delta E = E_{\rm max} - E_{\rm min}$  and  $E_{\rm max}$  and  $E_{\rm min}$  are the rest-frame energies of

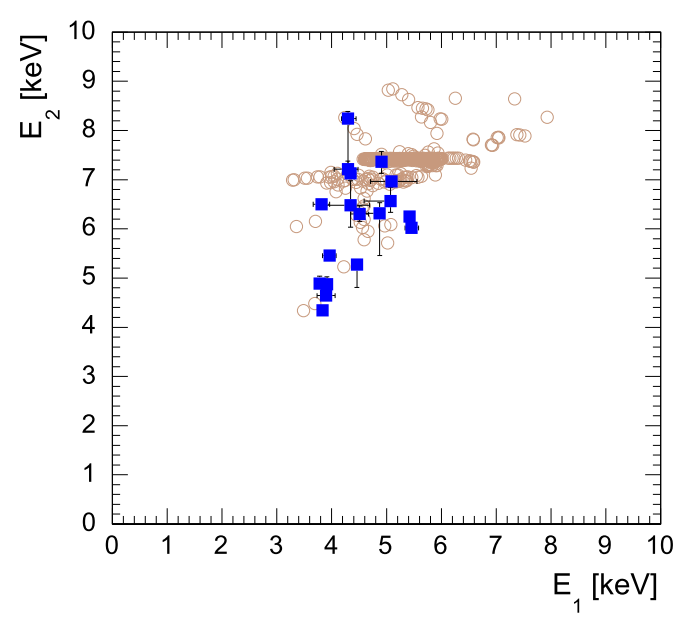


**Figure 13.** Scatter between the peak energies of simulated (open circles) and observed (solid squares) double-peaked line profiles. The simulations are for a black hole with a spin of a = 0.3 seen at an inclination of  $i = 82^{\circ}5$ .

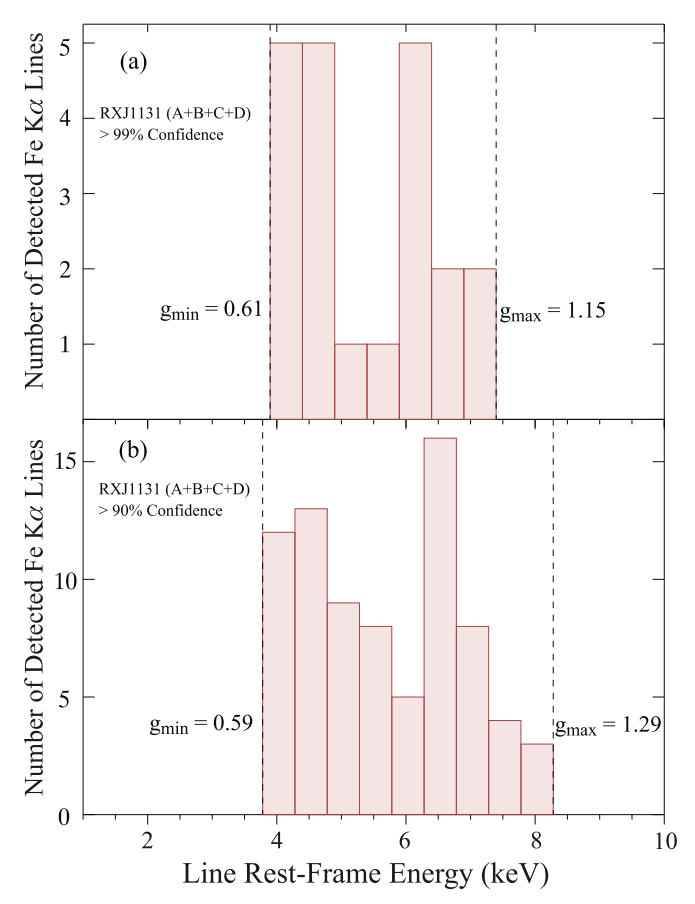


**Figure 14.** Distribution of the Fe  $K\alpha$  line energies for all images and all 38 epochs of data for RXJ1131. Only cases where the iron line is detected at >99% (a) and at >90% confidence (b) are shown. The vertical lines mark the extreme limits of the distribution used to determine upper limits on the ISCO and inclination angle.

the shifted lines. As we discussed in Section 3, our numerical simulations show that the peak energy of the  $\Delta E$  distribution depends strongly on the spin parameter. Specifically, our

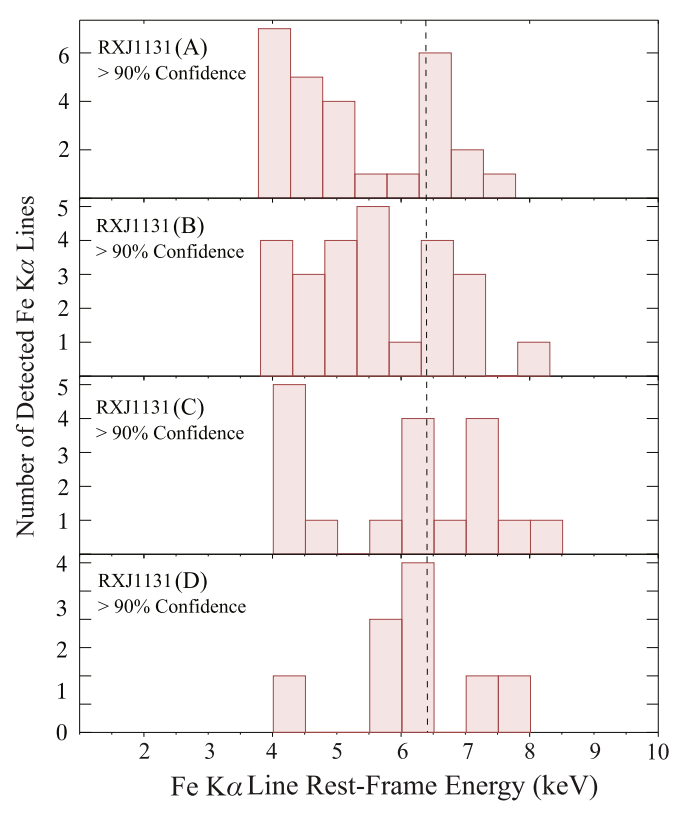


**Figure 15.** Distribution of the Fe K $\alpha$  line energies for the individual images A, B, C, and D and all 38 epochs of data for RXJ1131. Only cases where the iron line is detected at >90% confidence are shown.

simulations indicate that the  $\Delta E$  distributions of RX J1131–1231 for input spin parameters of a=0 and a=0.98 peak at  $1.8\pm0.2\,\mathrm{keV}$  and  $3.2\pm0.2\,\mathrm{keV}$ , respectively. We find that the maximum of the observed  $\Delta E$  distribution of RX J1131–1231 peaks at  $\sim$ 3.5  $\pm$  0.2 keV, implying a spin parameter of  $a\gtrsim0.8$ . Additional observations of RXJ1131 will provide more representative and complete g and  $\Delta E$  distributions and place tighter constraints on the disk inclination angle, the ISCO radius, and the spin.

#### 5. Discussion and Conclusions

Our systematic spectral analysis of all the available *Chandra* observations of lensed quasars RXJ1131, QJ0158, and SDSS1004 has revealed the presence of a significant fraction of lines blueshifted and redshifted with respect to the energy of the expected Fe  $\rm K\alpha$  fluorescence line. We interpret these energy shifts as being the result of ongoing microlensing in all of the images. This seems logical given the prior detections of microlensing of the optical, UV (e.g., Blackburne et al. 2006; Fohlmeister et al. 2007; Morgan et al. 2008; Motta et al. 2012; Fian et al. 2016), and X-ray continuum (e.g., Chartas et al. 2009, 2012, 2016; Dai et al. 2010; Chen et al. 2011, 2012) in all three sources. We consider several alternative scenarios and examine whether they can explain the observed shifted iron lines.

(a) Nonmicrolensed emission from hot spots and patches from an inhomogeneous disk. Redshifted Fe emission lines have been reported in observations of a few bright Seyfert galaxies (i.e., Iwasawa et al. 2004; Turner et al. 2004, 2006; Miller et al. 2006; Tombesi et al. 2007). Correlated modulation of redshifted Fe line emission and the continuum were reported in NGC 3783 (Tombesi et al. 2007). Specifically, the spectrum

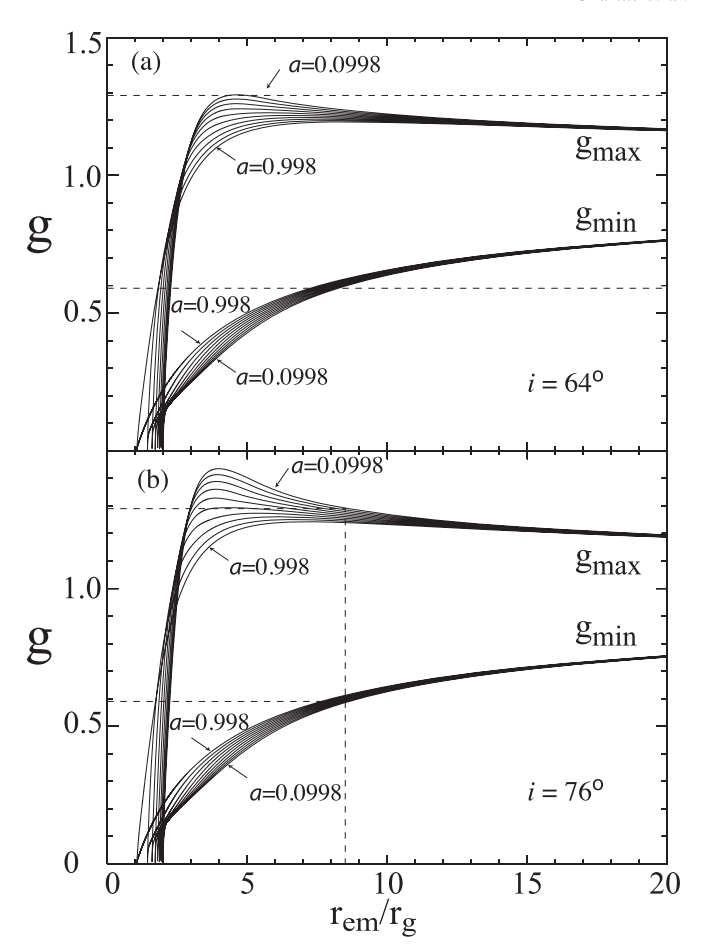


**Figure 16.** Extremal shifts of the Fe K $\alpha$  line energy for spin values ranging between 0.098 and 0.998 in increments of 0.1. Horizontal lines represent the observed values of  $g=E_{\rm obs}/E_{\rm rest}$  of the most redshifted and blueshifted Fe K $\alpha$  lines from all 38 epochs and all images of RXJ1131. The extreme g values are for Fe K $\alpha$  lines detected at >90% confidence. (a) The extremal shifts for an inclination angle of  $i=64^\circ$ . (b) The extremal shifts for an inclination angle of  $i=76^\circ$ . The inner radius of the accretion disk is constrained to be  $r_{\rm ISCO} < 8.5 r_{\rm g}$ .

of NGC 3783 shows, in addition to a core Fe K $\alpha$  line at 6.4 keV, a weaker redshifted wing and redshifted Fe emission line component. The redshifted line and wing appear to show an intensity modulation on a 27 ks timescale similar to that of the 0.3–10 keV continuum. Tombesi et al. (2007) argue that the lack of Fe line energy modulation disfavors the orbiting flare/ spot interpretation for NGC 3783. We note that the relative intensity of the core Fe line to the redshifted Fe line component in NGC 3783 is about a factor of 9. The core Fe K $\alpha$  line has an EW of about  $120 \, \text{eV}$  and the redshifted line of  $\sim 13 \, \text{eV}$ . Redshifted lines are also reported to be present in the spectrum of Mrk 766 (Turner et al. 2004, 2006), where a weak component of the Fe line with an EW of  $15^{+6}_{-5}$  eV shows a periodic variation of photon energy. The proposed scenario by Turner et al. (2006) is that the energy variation is caused by a hot spot on the disk within  $\sim 100 r_{\rm g}$  orbiting with a period of about ∼165 ks. The average spectrum of Mrk 766 shows a broad iron line center near 6.7 keV with an EW of about 90 eV (possibly from reflection off an ionized disk) and a narrower component at 6.4 keV (possibly from reflection from distant material).

The shifted Fe lines detected in our gravitationally lensed quasar sample have very different properties from those reported

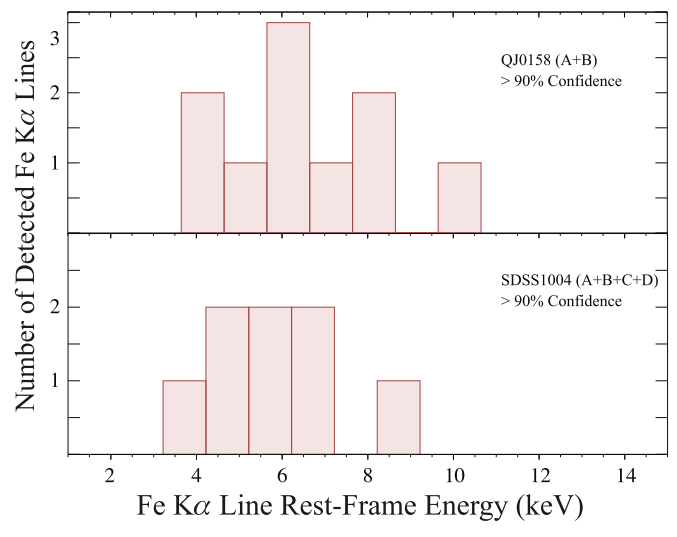


**Figure 17.** Distribution of the Fe  $K\alpha$  line energies for all images of QJ0158 (top, 12 epochs) and SDSS1004 (bottom, 10 epochs). Only cases where the iron line is detected at >90% confidence are shown.

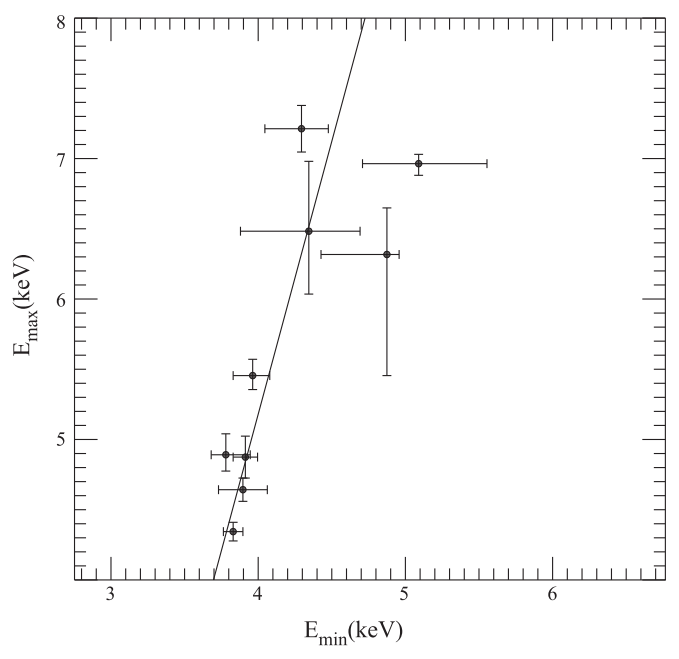


**Figure 18.** Rest-frame energies of the shifted double Fe lines detected in image A of RXJ1131 at the >90% confidence level. We also show the straight-line least-squares fit to the data in the solid line.

in NGC 3783 and Mrk 766, while our our microlensing interpretation is consistent with the observed properties of the energy-shifted lines. Specifically, the EWs of the energy-shifted lines in the lensed quasar sample range from EW = 500 to 3000 eV compared to the EW = 13 eV and EW = 15 eV in the shifted lines detected in NGC 3783 and Mrk 766, respectively. Nonmicrolensed emission from hot spots and patches from an inhomogeneous disk lie below the detection threshold of the individual spectra of the lensed quasars. The nonmicrolensed emission from the Fe K $\alpha$  line at 6.4 keV is not detected in individual spectra of RX J1131–1231, but is detected in the stacked spectra of RX J1131–1231 with  $E = 6.36^{+0.07}_{-0.08}$  keV and EW = 154 $^{+70}_{-80}$  eV (Chartas et al. 2012, 2016). In the cases of Seyfert galaxies NGC 3783 and Mrk 766, the redshifted weak

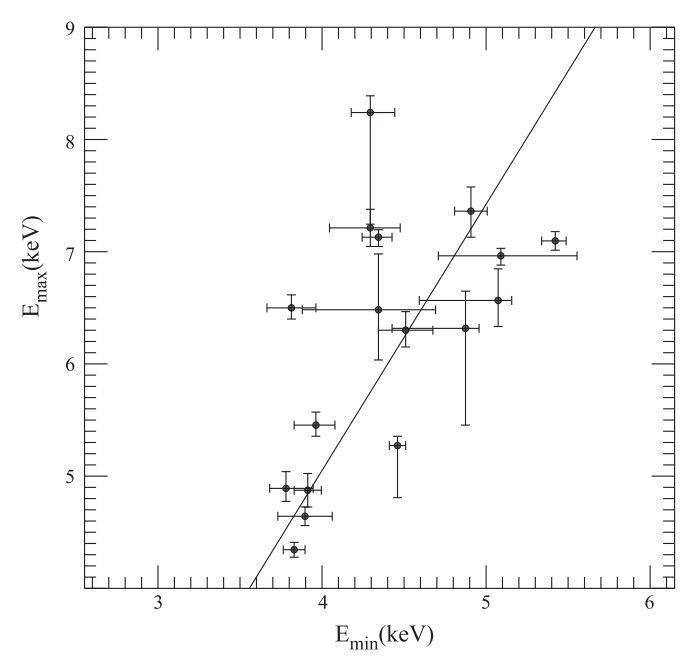


**Figure 19.** Rest-frame energies of the shifted double Fe lines detected in all images of RXJ1131 at the >90% confidence level. We also show the straightline least-squares fit to the data in the solid line.

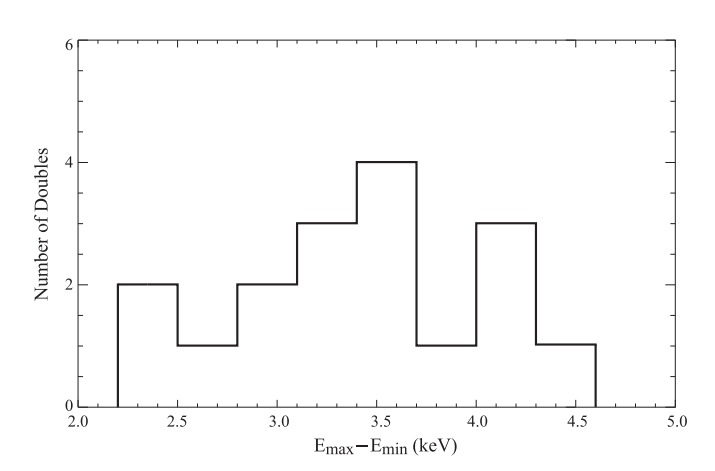


**Figure 20.** Observed distribution of the rest-frame energy separations for shifted double Fe lines detected in all images of RXJ1131 at the >90% confidence level.

Fe lines are always accompanied by a significantly stronger core component near 6.4 keV, whereas this is not the case for the lensed quasars. Another point supporting the microlensing interpretation is the detection of a significant number of double lines in RX J1131–1231, as predicted in our numerical simulations of magnification caustics crossing an accretion disk. The intensities of these doubles are not consistent with nonmicrolensed Fe emission from hot spots and patches from an inhomogeneous disk.

- (b) Possible intrinsic absorption mimicking two apparent lines in RX J1131–1231. Our analysis of the  $4 \times 38$  spectra of RX J1131–1231 does not find any significant intrinsic absorption of the continuum spectra (Chartas et al. 2012), and there are no absorption lines detected in the spectra that contain doubles.
- (c) Possible ionization of accretion disk. In Figure 9 of Chartas et al. (2012) we showed a stacked spectrum of image C

**Table 8**Correlation Results of RX J1131–1231

TEST	QUANTITY I	QUANTITY II	$N_{\mathrm{sample}}^{\mathrm{a}}$	STATISTIC	CHANCE PROBABILITY
Spearman's (ρ)	$E_{\min}^{^{b}}$	$E_{\max}^{b}$	9	0.78	0.015
Kendalls's $(\tau)$	$E_{\min}^{^{b}}$	$E_{ m max}^{}$	9	0.61	0.022
Spearman's $(\rho)$	$E_{\min}^{\ \ c}$	$E_{\mathrm{max}}^{}}$	17	0.52	0.032
Kendalls's $(\tau)$	$E_{\min}^{^{\mathbf{c}}}$	$E_{ m max}^{}$	17	0.39	0.031
Spearman's (ρ)	$\mathrm{EW}_{\mathrm{Fe}}$	g	78	0.42	$1.6 \times 10^{-4}$
Kendalls's $(\tau)$	$\mathrm{EW}_{\mathrm{Fe}}$	g	78	0.28	$2.4 \times 10^{-4}$
Spearman's (ρ)	$N_{ m Fe}$	$N_{ m cont}$	78	0.69	$4.4 \times 10^{-12}$
Kendalls's $(\tau)$	$N_{ m Fe}$	$N_{ m cont}$	78	0.50	$<1 \times 10^{-12}$

**Notes.** Spearman's ( $\rho$ ) and Kendalls's ( $\tau$ ) rank correlations of two sample populations labeled QUANTITY II.

of RXJ1131 covering a period of about seven years filtering for epochs where microlensing was not significant in this image. A significant Fe  $K\alpha$  line is detected in the stacked spectrum of image C at an energy of  $6.36^{+0.07}_{-0.08}$  keV with an EW of  $154^{+70}_{-80}$  eV. This detected energy of the Fe  $K\alpha$  line in image C is consistent with the presence of a nonionized disk in RXJ1131. The expected energy of the iron line for an ionized disk would be 6.67 keV (He-like Fe) or 6.97 keV (H-like iron).

We conclude that the variability in the flux and energy of the iron line detected in the *Chandra* observations of RXJ1131, QJ0158, and SDSS1004 is due to ongoing microlensing of all of the images.

Large magnification events are typically inferred from the departure of the time-delay-corrected flux ratios of images from a constant, and images that show significant uncorrelated variability are significantly affected by microlensing. We note, however, that a relatively large number of the shifted Fe lines were found in images that do not show significant variability of their flux ratios or significant uncorrelated variability. This implies that the line profiles found using stacked spectra taken over multiple epochs, even when excluding spectra from images that show variability of their flux ratios, are also distorted by microlensing, and that applying the relativistic Fe K $\alpha$  method as used to analyze local Seyferts will not lead to reliable results. Any apparent broadening of the iron line in a stacked spectrum of a lensed quasar is a combination of both microlensing and the relativistic blurring seen in unlensed Seyferts. The average stacked spectrum of a microlensed quasar differs significantly, especially near the Fe K $\alpha$  line, from that of an unlensed one. The main reason for this difference is that the reflection and direct (coronal) components of a stacked spectrum of a microlensed quasar are not a simple, uniform magnification of the reflection and direct components of unlensed quasars. Caustic magnification patterns (e.g., see Figures 12-16 of Kochanek 2004) move along a certain direction with respect to the source (that differs between images), and the caustic magnification is not uniform. Stacked spectra of lensed quasars will thus not result in uniformly magnified reflection and direct spectral components but will produce spectra that have been selectively magnified by caustics moving along a limited range of caustic crossing angles. The caustic magnification factor K will also vary between caustic crossings, making the stacked spectrum deviate even more than a uniformly magnified quasar spectrum.

We summarize our main conclusions from the X-ray observations of RXJ1131, QJ0158, and SDSS1004 as follows:

- (1) Redshifted and blueshifted Fe lines with rest-frame EWs ranging between 500 and 3000 eV are detected in the individual epoch spectra of lensed quasars RXJ1131, QJ0158, and SDSS1004. We interpret these energy shifts as the result of microlensing of Fe line emission within  $\sim$ 20  $r_{\rm g}$  of the black hole.
- (2) The g distribution of the observed energy shifts in RXJ1131 is compared to analytic and numerical models, and both models provide similar constraints on accretion disk parameter. Specifically, the maximum value of  $g_{\text{max}} = 1.29^{+0.04}_{-0.04}$ constrains the inclination angle to be  $i \gtrsim 76^\circ$ , and the minimum value  $g_{\min} = 0.59$  constrains  $r_{\rm ISCO} \lesssim 8.5 r_g$ . If we only consider energy shifts detected above the 99% confidence level, the upper limit on the ISCO radius is  $r_{\rm ISCO} \lesssim 8.5 r_g$  and the lower limit on the disk inclination angle is  $i \gtrsim 55^{\circ}$ . One of the strengths of the g-distribution method is that the energies of the shifted Fe lines are more robustly detected than the extreme weak red wings of the relativistic Fe K $\alpha$  line that are found mostly in nearby Seyfert galaxies. For example, the energies of the shifted lines are not sensitive to the modeling of the underlying continuum, while the shape of the relativistic Fe K $\alpha$  red wing is very sensitive to the continuum model. The g-distribution method can be applied to infer the inclination angles, ISCO radii, and spins of distant quasars, where the relativistic Fe K $\alpha$  red wing is typically too faint to constrain these parameters in distant quasars. One of the weaknesses of the g-distribution method is that there are additional model parameters related to describing the gravitational lens.
- (3) Several spectra show two shifted Fe lines, which we refer to as doubles. The peak energies of the doubles are moderately correlated. Our numerical simulations reproduce the double lines during caustic crossings, and we find that the distribution of the separations of the peak energies is strongly dependent on the spin parameter. The maximum of the observed  $\Delta E$  distribution of RX J1131–1231 peaks at  $\sim 3.5 \pm 0.2$  keV, suggesting a high spin parameter. Although a statistical analysis of the results still needs to be performed, inspection of the mean energy, peak energy, and shape of the distribution indicates a rather high value of the spin  $a \gtrsim 0.8$ . The available  $\Delta E$  distribution of RX J1131–1231 is sparsely populated, and additional observations are required to better constrain the peak energy of this distribution and infer the spin parameter more accurately.
- (4) We find several correlations in the microlensed spectra of RXJ1131, and the results are summarized in Table 8.

<sup>&</sup>lt;sup>a</sup> The number of elements in the sample.

 $<sup>^{\</sup>rm b}$  Rest-frame energies of the shifted double Fe lines in image A detected at the >90% confidence level.

<sup>&</sup>lt;sup>c</sup> Rest-frame energies of the shifted double Fe lines in all images detected at the >90% confidence level.

Specifically, we find a correlation between the rest-frame EW of the iron lines and the generalized Doppler shift parameter g of the iron line ( $\tau=0.28, P>99.9\%$ ). The flux of the shifted Fe line is found to be correlated with the flux of the continuum for Fe K $\alpha$  lines detected at >90% confidence in all images of RXJ1131 ( $\tau=0.5, P>99.9\%$ ). The energies of the doubles in image A are also found to be correlated ( $\tau=0.6, P>98\%$ ).

(5) Our numerical simulations of microlensing caustic crossings reproduce the observed distribution of energy of single and double shifts in microlensed spectra and predict the correlations observed in the spectra.

Scheduled future monitoring observations with *Chandra* of the lensed quasars RXJ1131, QJ0158, SDSS1004, and Q 2237 +0305 with sufficiently long exposure times to improve the significance of the detections will provide more representative and complete distributions of the generalized Doppler shift g values of the Fe K $\alpha$  line in these objects. The g-distribution method and modeling of doubles are expected to provide robust constraints on inclination angle, the ISCO radii, and spins of the black holes of these distant lensed quasars. With the Large Synoptic Survey Telescope coming online in the near future, we expect  $\sim$ 4000 new lensed systems to be discovered, opening up the possibility of measuring black hole and accretion disk parameters over a wide range of redshifts and quasar Eddington ratios  $L_{\rm Bol}/L_{\rm Edd}$ .

We acknowledge financial support from NASA via the Smithsonian Institution grants SAO GO4-15112X, GO3-14110A/B/C, GO2-13132C, GO1-12139C, and GO0-11121C. C.W.M. gratefully acknowledges support from NSF Award AST-1211146. C.S.K. is supported by NSF grant AST-1515876.

# Appendix Calculating the Generalized Doppler Shifts g

The generalized Doppler shifts g were calculated for the case of a spinning black hole (Kerr 1963) using the formalism described in Bardeen et al. (1972), Müller & Camenzind (2004), and Karas & Sochora (2010). The azimuthal velocity is

$$v_{\phi} = \tilde{\Omega} \frac{(\Omega - \Omega_0)}{\sqrt{\frac{\Delta \Sigma}{A}}},\tag{7}$$

where  $\tilde{\Omega}$  and  $\Omega_0$  are given by

$$\tilde{\Omega} = \sqrt{\frac{A}{\Sigma}} \sin \theta \quad \text{and} \tag{8}$$

$$\Omega_0 = \frac{2a}{A} r_g r. \tag{9}$$

For  $r > r_{\rm ms}$ , a Keplerian velocity profile is assumed, and

$$\Omega = \frac{r_g^{1/2}}{r^{3/2} + ar_o^{1/2}}. (10)$$

For  $r \leqslant r_{\text{ms}}$ , a constant specific angular momentum is assumed, and the angular velocity  $\Omega$  is given by

$$\Omega = \Omega_0 + \frac{\Delta \Sigma}{A} \tilde{\Omega}^{-2} \frac{\lambda_{\rm ms}}{1 - \Omega_0 \lambda_{\rm ms}},\tag{11}$$

where

$$\lambda_{\rm ms} = \frac{\widetilde{\Omega}_{\rm ms}^2 (\Omega_{\rm ms} - \Omega_{0,\rm ms})}{\left[\left(\frac{\Delta\Sigma}{A}\right) + \Omega_{0,\rm ms}\widetilde{\Omega}_{\rm ms}^2 (\Omega_{\rm ms} - \Omega_{0,\rm ms})\right]}.$$
 (12)

All quantities with the subscript ms are calculated at the marginal stable orbit.

For these calculations, we assumed the radial and toroidal velocity components  $v_r$  and  $v_\theta$  of the radiating plasma of the accretion disk in the zero angular momentum observer frame to be relatively small. For a given inclination angle i, the angle between the direction of the orbital velocity  $v_\phi$  of the plasma and our line of sight is assumed to range between a minimum and maximum value that will depend on the inclination angle i and the angle between the caustic direction of motion and the projection of our line of sight onto the disk plane.

#### References

```
Bardeen, J. M., Press, W. H., & Teukolsky, S. A. 1972, ApJ, 178, 347
Beheshtipour, B., Hoormann, J. K., & Krawczynski, H. 2016, ApJ, 826, 203
Blackburne, J. A., Kochanek, C. S., Chen, B., Dai, X., & Chartas, G. 2014,
   ApJ, 789, 125
Blackburne, J. A., Kochanek, C. S., Chen, B., Dai, X., & Chartas, G. 2015,
   ApJ, 798, 95
Blackburne, J. A., Pooley, D., & Rappaport, S. 2006, ApJ, 640, 569
Cackett, E. M., Zoghbi, A., Reynolds, Ĉ., et al. 2014, MNRAS, 438, 2980
Cash, W. 1979, ApJ, 228, 939
Chandrasekhar, S. 1960, Radiative Transfer (New York: Dover)
Chartas, G., Agol, E., Eracleous, M., et al. 2002, ApJ, 568, 509
Chartas, G., Falco, E., Forman, W., et al. 1995, ApJ, 445, 140
Chartas, G., Kochanek, C. S., Dai, X., Poindexter, S., & Garmire, G. 2009,
   ApJ, 693, 174
Chartas, G., Kochanek, C. S., Dai, X., et al. 2012, ApJ, 757, 137
Chartas, G., Rhea, C., Kochanek, C., et al. 2016, AN, 337, 356
Chen, B., Dai, X., Baron, E., & Kantowski, R. 2013, ApJ, 769, 131
Chen, B., Dai, X., Kochanek, C. S., et al. 2011, ApJL, 740, L34
Chen, B., Dai, X., Kochanek, C. S., et al. 2012, ApJ, 755, 24
Dai, X., Chartas, G., Agol, E., Bautz, M. W., & Garmire, G. P. 2003, ApJ,
  589, 100
Dai, X., & Kochanek, C. S. 2009, ApJ, 692, 677
Dai, X., Kochanek, C. S., Chartas, G., et al. 2010, ApJ, 709, 278
de Marco, B., Ponti, G., Uttley, P., et al. 2011, MNRAS, 417, L98
Dickey, J. M., & Lockman, F. J. 1990, ARA&A, 28, 215
Emmanoulopoulos, D., Papadakis, I. E., Dovčiak, M., & McHardy, I. M. 2014,
    MNRAS, 439, 3931
Edelson, R., Gelbord, J. M., Horne, K., et al. 2015, ApJ, 806, 129
Fabian, A. C., Parker, M. L., Wilkins, D. R., et al. 2014, MNRAS, 439,
Fabian, A. C., Rees, M. J., Stella, L., & White, N. E. 1989, MNRAS, 238,
Fabian, A. C., Zoghbi, A., Ross, R. R., et al. 2009, Natur, 459, 540
Faure, C., Anguita, T., Eigenbrod, A., et al. 2009, A&A, 496, 361
Fausnaugh, M. M., Denney, K. D., Barth, A. J., et al. 2016, ApJ, 821, 56
Fian, C., Mediavilla, E., Hanslmeier, A., et al. 2016, arXiv:1608.03831
Fohlmeister, J., Kochanek, C. S., Falco, E. E., et al. 2007, ApJ, 662, 62
Fohlmeister, J., Kochanek, C. S., Falco, E. E., Morgan, C. W., &
  Wambsganss, J. 2008, ApJ, 676, 761
García, J., Dauser, T., Reynolds, C. S., et al. 2013, ApJ, 768, 146
Garmire, G. P., Bautz, M. W., Ford, P. G., Nousek, J. A., & Ricker, G. R., Jr.
  2003, Proc. SPIE, 4851, 28
Hoormann, J. K., Beheshtipour, B., & Krawczynski, H. 2016, PhRvD, 93,
Iwasawa, K., Miniutti, G., & Fabian, A. C. 2004, MNRAS, 355, 1073
Kara, E., Alston, W. N., Fabian, A. C., et al. 2016, MNRAS, 462, 511
Kara, E., Cackett, E. M., Fabian, A. C., Reynolds, C., & Uttley, P. 2014,
```

Kara, E., Fabian, A. C., Cackett, E. M., Miniutti, G., & Uttley, P. 2013,

Keck, M. L., Brenneman, L. W., Ballantyne, D. R., et al. 2015, ApJ, 806, 149

MNRAS, 439, L26

MNRAS, 430, 1408

Karas, V., & Sochora, V. 2010, ApJ, 725, 1507

```
Kerr, R. P. 1963, PhRvL, 11, 237
Kochanek, C. S. 2004, ApJ, 605, 58
Kochanek, C. S., Dai, X., Morgan, C., et al. 2007, in ASP Conf. Ser. 371,
   Statistical Challenges in Modern Astronomy IV, ed. G. Jogesh Babu &
  E. D. Feigelson (San Francisco, CA: ASP), 43
Krawczynski, H. 2012, ApJ, 754, 133
Kulkarni, A. K., Penna, R. F., Shcherbakov, R. V., et al. 2011, MNRAS,
   414, 1183
Laor, A. 1991, ApJ, 376, 90
MacLeod, C. L., Morgan, C. W., Mosquera, A., et al. 2015, ApJ, 806, 258
Matt, G., Perola, G. C., & Piro, L. 1991, A&A, 247, 25
McKinney, J. C., Tchekhovskoy, A., Sadowski, A., & Narayan, R. 2014,
           , 441, 3177
Miller, L., Turner, T. J., Reeves, J. N., et al. 2006, A&A, 453, L13
Miller, L., Turner, T. J., & Reeves, J. N. 2009, MNRAS, 399, L69
Morgan, C. W., Hainline, L. J., Chen, B., et al. 2012, ApJ, 756, 52
Morgan, C. W., Kochanek, C. S., Dai, X., Morgan, N. D., & Falco, E. E. 2008,
     J, 689, 755
Morgan, C. W., Kochanek, C. S., Morgan, N. D., & Falco, E. E. 2010, ApJ,
   712, 1129
Mosquera, A. M., & Kochanek, C. S. 2011, ApJ, 738, 96
Mosquera, A. M., Kochanek, C. S., Chen, B., et al. 2013, ApJ, 769, 53
Motta, V., Mediavilla, E., Falco, E., & Muñoz, J. A. 2012, ApJ, 755, 82
Müller, A., & Camenzind, M. 2004, A&A, 413, 861
Noble, S. C., Krolik, J. H., Schnittman, J. D., & Hawley, J. F. 2011, ApJ,
   743, 115
Novikov, I. D., & Thorne, K. S. 1973, Black Holes, ed. C. DeWitt-Morette &
  B. S. DeWitt, (New York: Gordon and Breach), 343
Page, D. N., & Thorne, K. S. 1974, ApJ, 191, 499
Parker, M. L., Wilkins, D. R., Fabian, A. C., et al. 2014, MNRAS, 443,
Penna, R. F., Saowski, A., & McKinney, J. C. 2012, MNRAS, 420, 684
Planck Collaboration, Ade, P. A. R., Aghanim, N., et al. 2016, A&A, 594, A13
Pooley, D., Blackburne, J. A., Rappaport, S., & Schechter, P. L. 2007, ApJ, 661, 19
Pooley, D., Rappaport, S., Blackburne, J. A., Schechter, P. L., & Wambsganss, J.
   2012, ApJ, 744, 111
Popović, L. Č., Jovanović, P., Mediavilla, E., et al. 2006, ApJ, 637, 620
```

```
Press, W. H., Teukolsky, S. A., Vetterling, W. T., & Flannery, B. P. 1992,
   Numerical Recipes in FORTRAN (2nd ed.; Cambridge: Cambridge Univ.
  Press)
Protassov, R., van Dyk, D. A., Connors, A., Kashyap, V. L., &
  Siemiginowska, A. 2002, ApJ, 571, 545
Reis, R. C., Reynolds, M. T., Miller, J. M., & Walton, D. J. 2014, Natur, 507, 207
Reynolds, C. S. 2014, SSRv, 183, 277
Reynolds, C. S., & Begelman, M. C. 1997, ApJ, 488, 109
Reynolds, C. S., & Fabian, A. C. 2008, ApJ, 675, 1048
Reynolds, C. S., & Nowak, M. A. 2003, PhR, 377, 389
Reynolds, M. T., Walton, D. J., Miller, J. M., & Reis, R. C. 2014, ApJL,
  792, L19
Ross, R. R., & Fabian, A. C. 2005, MNRAS, 358, 211
Sądowski, A. 2016, MNRAS, 459, 4397
Schneider, P., Ehlers, J., & Falco, E. E. 1992, Gravitational Lenses, XIV
   (Berlin: Springer)
Schnittman, J. D., & Krolik, J. H. 2009, ApJ, 701, 1175
Schnittman, J. D., & Krolik, J. H. 2010, ApJ, 712, 908
Shakura, N. I., & Sunyaev, R. A. 1973, A&A, 24, 337
Shappee, B. J., Prieto, J. L., Grupe, D., et al. 2014, ApJ, 788, 48
Sim, S. A., Proga, D., Kurosawa, R., et al. 2012, MNRAS, 426, 2859
Sluse, D., Hutsemékers, D., Courbin, F., Meylan, G., & Wambsganss, J. 2012,
   A&A, 544, A62
Tewes, M., Courbin, F., Meylan, G., et al. 2013, A&A, 556, A22
Tombesi, F., de Marco, B., Iwasawa, K., et al. 2007, A&A, 467, 1057
Turner, T. J., Kraemer, S. B., & Reeves, J. N. 2004, ApJ, 603, 62
Turner, T. J., Miller, L., George, I. M., & Reeves, J. N. 2006, A&A, 445, 59
Uttley, P., Cackett, E. M., Fabian, A. C., Kara, E., & Wilkins, D. R. 2014,
   A&ARv, 22, 72
Vasudevan, R. V., Fabian, A. C., Reynolds, C. S., et al. 2016, MNRAS,
   458, 2012
Volonteri, M., Sikora, M., Lasota, J.-P., & Merloni, A. 2013, ApJ, 775, 94
Walton, D. J., Reynolds, M. T., Miller, J. M., et al. 2015, ApJ, 805, 161
Wambsganss, J. 2006, arXiv:astro-ph/0604278
Witt, H. J., Kayser, R., & Refsdal, S. 1993, A&A, 268, 501
Wyithe, J. S. B., Agol, E., & Fluke, C. J. 2002, MNRAS, 331, 1041
Wyithe, J. S. B., Webster, R. L., & Turner, E. L. 2000, MNRAS, 318, 762
```